Doctoral Dissertation

Ultrafast All-Optical Analog-to-Digital Conversion and Logic Operations Using Nonlinear Optical Loop Mirrors with Multi-Period Transfer Function

Yuji Miyoshi

Division of Electrical, Electronic and Information Engineering

Graduate School of Engineering

Osaka University

July 2008

Preface

This thesis presents a study on ultrafast all-optical analog-to-digital (A/D) conversions and logic operations, which aim to be free from the speed limitation of electrical devices. The content of the dissertation is based on researches that were carried out during my Ph. D. course at the Division of Electrical, Electronic and Information Engineering, Graduate School of Engineering, Osaka University. The dissertation is organized as follows:

Chapter 1 is a general introduction, which gives background and the purpose of the study. In the future optical communication systems, to increase the bit rate of optical transmission systems, ultrafast A/D conversion is required for dispersion compensation techniques and advanced modulation format using digital signal processing, and to provide flexible photonic network, ultrafast all-optical logic gate is required for signal processing in photonic routers.

Chapter 2 introduces optical quantizing and coding using multi-period transfer functions of nonlinear optical loop mirror (NOLM). In previous work, the number of bit resolution of optical A/D conversion was only 3-bit, which was not sufficient for optical communication systems. We investigated numerical design considerations of NOLM, which is a key to the optical quantizing and coding. We consequently demonstrated a record, nearly 4-period transfer function for a control pulse width of approximately 2 ps capable of the 4-bit A/D conversion at the sampling rate of 100 GS/s. Finally we demonstrated nearly 8-period transfer function of a NOLM. In future, the 5-bit A/D conversion will be possible.

Chapter 3 proposes a split-and-delay technique for simplifying of the multi-bit A/D conversion. Detailed design issues of the encoder considering for the counter-propagating effects in the case of slow and fast varying analog signals are also discussed. With this design technique, the sampling rate and the resolution of A/D converter can be easily changed, and the convenience of the all-optical A/D converter increases. We have succeeded in experimental demonstration of our proposed scheme to realize the quantizing and coding of 3-bit A/D conversion at the sampling rate of 10 GS/s.

Chapter 4 proposes a versatile all-optical logic gate based on multi-periodic transfer function of a NOLM. We have shown that the proposed scheme can perform all sixteen two-input logic operations only by adjusting PCs and VOAs without changing the configuration. The flexibility and ultrafast operation are expected to support the digital signal processing in photonic router in future optical communication systems. We have also experimentally demonstrated all-optical AND, NAND, OR, NOR, XOR, and XNOR operations at a processing speed of 40 Gbit/s. It has been found that control and probe pulses with short temporal widths and a carefully designed wavelength allocation are required for realizing a ultrafast logic gate. We show the feasibility of the processing speed and the extinction ratio up to 350 Gbit/s and 13.7 dB by numerical simulation, respectively.

From all the obtained result, it is concluded that, the proposed all-optical A/D conversion and logic

operations have the feasibilities of ultrafast and flexible operations. Each proposed technique is expected to support several digital signal processing for advance future optical communication networks.

All the results described in the dissertation were published in OSA Journal of Optics Express, IEEE/OSA Journal of Lightwave Technology, Proceedings of the 31st, 32nd and 33rd European Conference on Optical Communication (ECOC 2005, ECOC 2006 and ECOC 2007), and Proceeding of the 2007 IEEE MTT-S International Microwave Symposium (IMS 2007).

Yuji Miyoshi

Osaka Japan
July 2008

Acknowledgements

This research has been carried out during my tenure of doctoral course at the Division of Electrical, Electronic and Information Engineering, Graduate School of Engineering, Osaka University, under the guidance of Prof. Ken-ichi Kitayama.

I would like to express my deepest sense of appreciation to Prof. Ken-ichi Kitayama, for his instruction, continuous encouragement, valuable discussions, and careful review during the period of this research. His keen sight and a wealth of farsighted advice have always provided me precise guiding frameworks of my research. I have learned from many valuable lessons through my research in Osaka University, which I have further developed my abilities.

I am profoundly indebted to Prof. Kyo Inoue for his comments and suggestions, which have improved this dissertation. I am much indebted to Associate Prof. Akihiro Maruta fruitful suggestions and careful review in this dissertation.

I am much indebted to Prof. Zen-ichiro Kawasaki, Prof. Tetsuya Takine, Prof. Shozo Komaki, Prof. Noboru Babaguchi, Prof. Seiichi Sampei, Prof. Kenji Taniguchi, Prof. Shinsuke Hara of Osaka City University and all academic lectures at Division of Electrical, Electronic and Information Engineering, Osaka University for the giving me sufficient backgrounds for this dissertation.

I am also grateful to Associate Prof. Masayuki Matsumoto, and Associate Prof. Hiroyuki Toda of Doshisya University for their kind attentions and assistances.

I wish to express my sincere thanks to Dr. Shu Namiki of the National Institute of Advanced Industrial Science and Technology (AIST), Dr. Takashi Inoue, Mr. Hideaki Tobioka of FITEL Photonics Laboratory, the Furukawa Electric Co., Ltd and, and Hiroshi Nagaeda of the Trimatiz, Ltd.

I would like to express my gratitude to all the past and present colleagues in the Photonic Network Laboratory, Division of Electrical, Electronic and Information Engineering, Graduate School of Engineering, Osaka University. They have always provided me encouragement and friendship. I thank Dr. Kensuke Ikeda, and Mr. Seiki Takagi who collaborated on the study provided in this dissertation with me, for various fruitful and helpful discussions. Special thanks go to Dr. Shoichiro Oda, Dr. Nobuyuki Kataoka, Dr. Hochul Ji, Dr. Juan Jose Vegas Olmos, Dr. Shaowei Huang, Dr. Christos Tsekrekos, Dr. Kozicki Bartlomiej, Ms. Marsden Adelys, Mr. Mohammad Faisal, Mr. Suresh Malinda Nissanka, Mr. Tetsuya Nakamura, Mr. Katsuya Muraoka, Mr. Tomochika Kanou, Mr. Naoki Nakagawa, Mr. Takahiro Kodama, Mr. Shougo Tomioka, and Mr. Shinji Tomofuji for valuable suggestions and hearty friendship.

I wish to acknowledge the Japan Society for Promotion of Science (JSPS) Research Fellowships for their grants and financial supports.

Finally I would like to thank my family for their deep understanding, unwavering love, patience, and support during the period of my education.

Contents

Chapter 1

Introduction

1.1 Demand of Ultrafast Signal Processing

An analog-to-digital (A/D) conversion is fundamental signal-processing technology, which serves as a front-end for the digital signal processing and analog signals. Analog-to-digital (A/D) conversion is one of the most fundamental functions in signal-processing technology because it converts input signals, which are essentially analog, into digital code sequences such that the input signals can be processed in a highly sophisticated manner through various digital signal-processing devices.

In recent years, high-speed A/D converters have been developed to support optical communications, radio communications with ultra-wide-band (UWB) technology, wide-band radar, radio astronomy and various measuring equipments [1-5]. Figure 1.1 graphically represents several different applications of A/D converters and their associated resolution and frequency requirements [6]. Particularly, ultrafast A/D conversions may find a wide variety of applications in the near future, including pre-processing of electrical dispersion compensation (EDC) in high-speed optical fiber communication systems [3-5]. The resolution for EDC is modest required around 5 or 6-bit, and the sampling rate is same or twice as the bit rate [4, 5].

On the other hand, several ultrafast optical logic gates are studied in optical communication systems. To increase the bit rate of an optical transmission system, ultrafast optical AND gates have been studied for an optical time division demultiplexer [7]. Also, in future photonic burst and packet switch networks, the photonic routers are expected to handle XOR operations for optical label swapping and header reconfiguration [8-10]. These applications require ultrafast logic operations in optical-time-division-multiplex (OTDM) communication system. Generally speaking, the realization of various logic operations for ultrafast signals is essential for coming future applications.

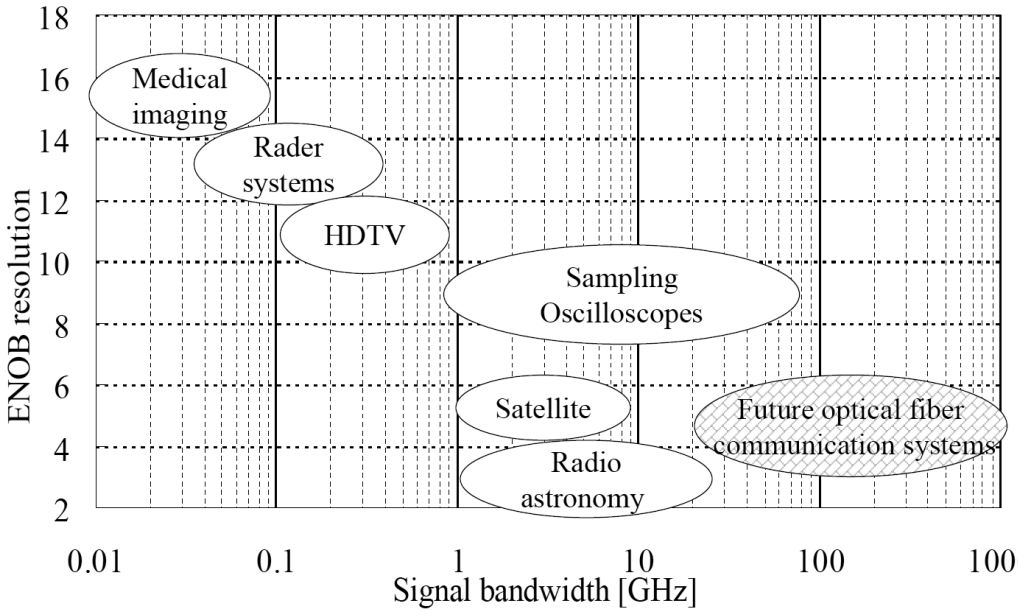

Fig. 1.1 Applications of A/D converters and their corresponding resolution and signal bandwidth requirements.

1.2 Fundamentals of A/D Conversion

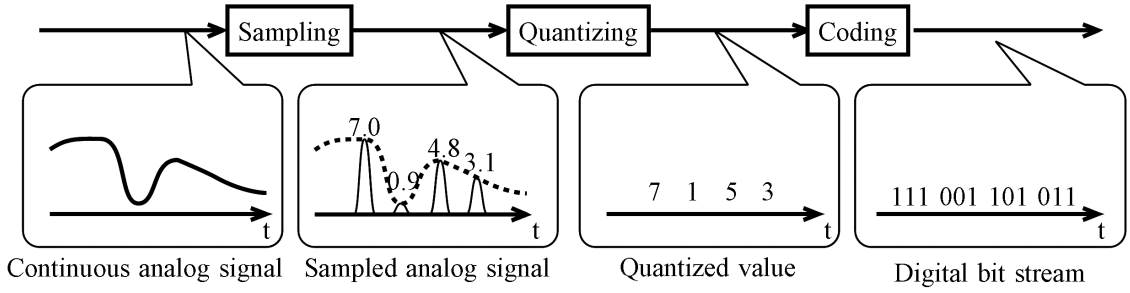

Fig. 1.2 Block diagram of A/D conversion.

The block diagram of A/D conversion is shown in Fig. 1.2. The A/D conversion consists of sampling, quantizing and coding. Sampling is to convert continuous analog signal into a discrete signal in the time domain. Quantizing is to convert the analog amplitude of the sampled signal into a discrete value by thresholding. Coding is to assign binary digits with according to a rule. The sampling rate and number of quantized levels are the most of properties of an A/D converter. Generally, a 2^N-level A/D converter is called a N-bit A/D converter. In this section, we introduce limitations of electrical A/D conversion, and possibility of a photonic A/D converter.

1.2.1 Limitations of Electrical A/D Conversion

The amplitude resolution of an A/D converter over the sampling rate of 100 MSamples/s depends on sampling jitter and comparator bandwidth [11]. The sampling jitter induces the amplitude error of a sampled analog signal, because the analog signal is not sampled at precise time. The comparator with insufficient bandwidth cannot decide the correct quantized level due to the transient response of an input signal. Therefore, the effective number of bit (ENOB) resolution decreases with the frequency of an input analog signal or sampling rate, as shown in Fig. 1.3 [11]. Electrical analog-to-digital (A/D) conversion operating at 3-bit, 40 Giga Samples per second (GS/s) was reported in 2004 [1]. The ENOB resolution is 2.30 bit at the input frequency of 9.99975 GHz. In typical high-performance electrical A/D conversion, the sampling jitter and comparator bandwidth ranges from 0.1 ps to 2 ps and 50 GHz to 150 GHz [12]. The resolution is limited to 3.5 ENOB at the signal bandwidth of 10 GHz with to the case of comparator bandwidth of 150 GHz. Time interleaved A/D conversions have been studied to overcome the limitation of comparator bandwidth. However, the ENOB resolution of time interleaved A/D converters is limited by the temporal jitter and the bandwidth of a sampling-and-hold circuit. The ENOB resolution of a time interleaved A/D converter reported in 2003 was 4.6 bit at a signal bandwidth of 6 GHz [13].

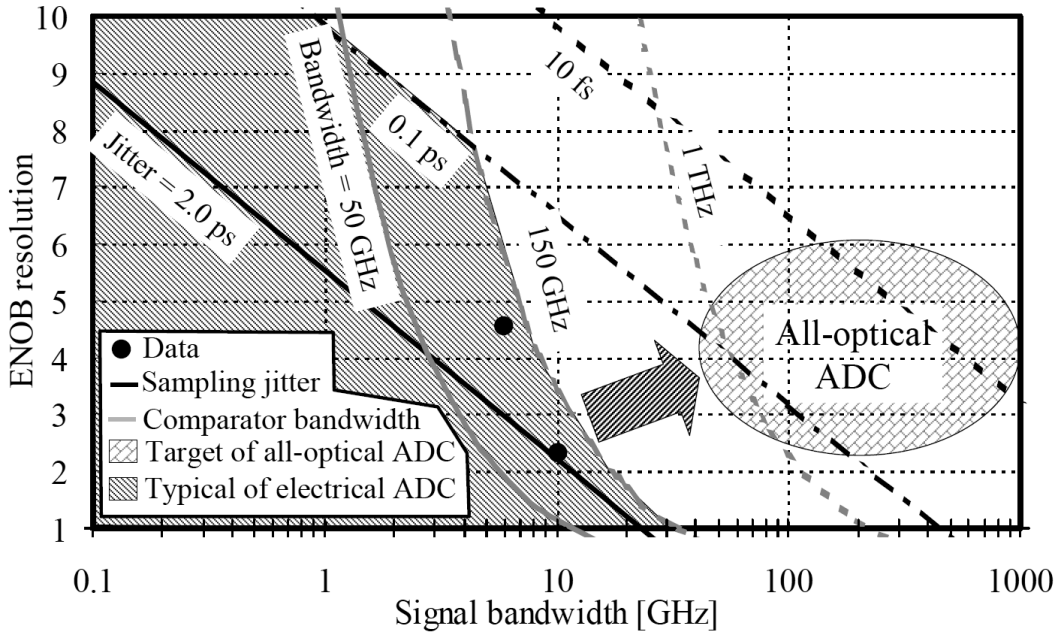

Fig. 1.3 Effective number of bit (ENOB) of resolution versus signal bandwidth with different sampling jitter and comparator bandwidth [1, 11-13].

1.2.2 All-Optical A/D Conversion

All-optical A/D conversion has a potential to overcome the above-mentioned limitation of electrical A/D conversion, because the timing jitter in the tens-femtoseconds regime is available by mode-locked laser technology, and the response time of Kerr effect in silica is the femtoseconds regime [14, 15]. Therefore, it is possible to operate multi-bit A/D conversion at the sampling rate of several hundreds GS/s.

Optical sampling in optical A/D conversion has been already realized by the methods of using a nonlinear optical loop mirror (NOLM) [16], four wave mixing (FWM) [17], etc. Several optical interleaved A/D converter using optical sampling, optical temporal demultiplexing and M-array electrical A/D converters have been proposed [18, 19], where M is the number of A/D converters. These schemes can use a low jitter optical source for sampling, and electrical A/D converters operate at a rate reduced by the factor M from the sampling rate. However, these schemes are required many high-speed electrical A/D converters for ultrafast A/D conversion. Therefore, these schemes lead to large-scale and high-cost implementation. Another approach based on a photonic time stretch technique was proposed, and an effective sampling rate of 1 TS/s has been achieved [20]. However, this scheme also requires many high-speed photo detectors and electrical A/D converters for continuous time measurement. To realize ultrafast A/D conversion, photonic quantizing and coding would be an ultimate solution.

An electro-optic quantizing and coding scheme was proposed in 1970s [21]. In this scheme, the electrical analog signal is converted into an optical digital signal using multi-period transfer functions of electro-optic modulators. The advantage of this scheme is that only N interferometers and N photo detectors are needed for N-bit A/D conversion. In 1999, an all-optical quantizing and coding scheme using periodic transfer functions of optical interferometer was proposed [22]. However, this scheme can measure only impulse-like signals, because a nonlinear optical loop mirror (NOLM) is practically used as the interferometer. When a continuous signal is launched into a NOLM, the NOLM dose not work due to a counter-propagating effect and the high average power of input signals [23]. Therefore, the input analog signals have to be converted into impulse-like signal by optical sampling. Moreover, to the best of my knowledge, over 2-period transfer function of a NOLM capable of 3-bit A/D conversion has been never reported [22, 24, 25]. However, the reported resolutions were not sufficient for optical communication systems. To realize all-optical A/D conversion, we have studied optical quantizing and coding scheme using multi-period NOLMs to convert into optical digital signal from sampled optical signals, and investigated the design of the

NOLM for improving the resolution.

1.3 All-Optical Logic Operation

All-optical logic operation has been studied to realize ultrafast logic operation, and to decrease the cost of photonic routers in future photonic networks by removing optical-to-electrical (O/E) conversion and electrical-to-optical (E/O) conversion.

Several approaches have been proposed to realize all-optical logic gates using semiconductor optical amplifiers (SOA) and highly nonlinear optical fibers (HNLF) [26-28]. The schemes using HNLF have advantages in that ultrafast optical signals can be processed through the femtosecond response of Kerr effect in silica [15]. However, HNLF tend to be large in size if integration is attempted, in contrast to those using integrated SOAs. Therefore, in order to be useful with such a difficulty of the HNLF-based schemes, one must seek a scheme such that one fixed configuration can provide as many logic operations as possible.

In order to provide flexibility, and to simplify the configuration, variable logic gates capable of some logic operations have been proposed [27-29]. To provide more flexibility with ultrafast operation, we propose a versatile all-optical logic gate using NOLM that is capable of all two-input logic operations without changing the configuration.

1.4 Overview of the Thesis

In the following chapters, introduction of fundamentals of photonic analog-to-digital conversion and design consideration of multi-period nonlinear optical loop mirror are described in Chapter 2, a simplified photonic analog-to-digital converter using the split-and-delay technique is proposed in Chapter 3, and a ultrafast versatile logic gate is proposed in Chapter 4:

Chapter 2 introduces a photonic quantizing and coding scheme using periodical transfer functions, and investigates design issues of NOLM with multi-period transfer function. To realize the optical quantizing and coding, the multi-period transfer function is indispensable. The influences of nonlinearity and group velocity dispersion on NOLM are discussed.

Chapter 3 proposes a split-and-delay technique and discusses the influence of counter-propagating effect with split-and-delay technique. The optical quantizing and coding scheme in Chapter 2 require 2N NOLMs for a N-bit photonic quantizing and optical coding. Therefore, the hardware constraint to

high-resolution or multi-bit quantizing is an issue to be solved. With this technique, the sampling rate and the resolution of A/D converter can be easily changed, and the convenience of the all-optical A/D converter increases. The split-and-delay technique realizes a N-bit photonic A/D converter using a single cascaded NOLM.

Chapter 4 proposes and demonstrates a versatile all-optical logic gate using NOLM that is capable of all two-input logic operations without changing the configuration. This scheme provides all two-input logic operations only by adjusting polarization controllers (PCs) and variable optical attenuators (VOAs), without changing the configuration. Then, we discuss the limitation of the processing speed due to dispersion effects and undesirable nonlinear effects in HNLF.

Chapter 5 summarizes all the results and concludes this thesis.

Chapter 2
Fundamentals of All-Optical Analog-to-Digital Conversion and Multi-Period Nonlinear Optical Loop Mirror

2.1 Introduction

In this chapter, we introduce an optical quantizing and coding scheme for an all-optical analog-to-digital (A/D) conversion and investigate design issues of a nonlinear optical loop mirror (NOLM), which is a key to the optical quantizing and coding. The All-optical A/D conversion is a potential break-through to overcome the limitations of the electronic A/D converters.

In Section 2.2, an optical quantizing and coding scheme using periodical transfer function is introduced. In Section 2.3, we review the principle of a NOLM. In Sections 2.4 and 2.5, we investigate design issues of a NOLM with multi-period transfer function.

2.2 Optical Quantizing and Coding Scheme Using Multi-period Transfer Function

We have studied an all-optical quantizing and coding scheme for ultrafast A/D conversion, using periodical transfer functions of NOLMs [24,25]. This scheme is based on the Taylor scheme [21]. Figure 2.1 shows the block diagram of the all-optical A/D conversion. This A/D converter consists of a sampler, a splitter, N-encoders and N-thresholders for N-bit A/D conversion.

As shown in Fig. 2.1, input analog optical signal is firstly sampled by optical sampling technique. The sampled optical analog signal is branched to N-pulses by splitter. The split pulses are inputted into N-encoders with different periodical transfer functions, respectively. The encoders have transfer functions for quantizing and coding, and the output code is the Gray Code characterized by only 1-bit changing between adjacent codes. Each encoder has a transfer function with different number of periods for quantizing and coding. The #n encoder must have the 2^{n-2} periods transfer function (n=1, 2, ~, N). The example of the Gray code is shown upper side of Fig. 2.2. In order to realize 3-bit A/D conversion with the Gray code, encoders #1, #2 and #3 have half-, single- and two-period transfer functions, respectively, as shown in the lower side of Fig. 2.2. Each encoder switches a sampled analog pulse into digital signal with the Gray code correspond to intensity of sampled analog pulse by the transfer function. Moreover, the thresholders improve the extinction ratio of the transfer function by rejecting residual "0" pulses and limiting excessive "1" pulses.

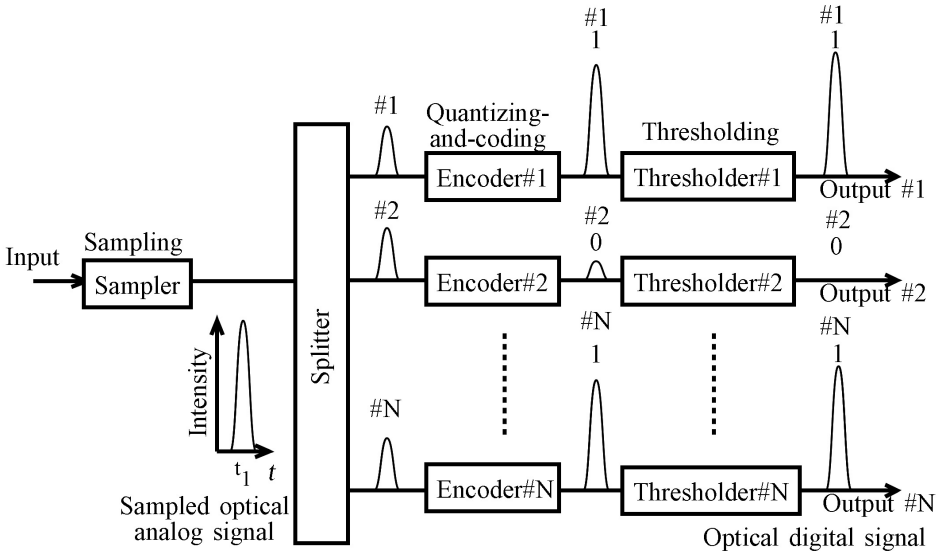

Fig. 2.1 Block diagram for all-optical A/D conversion.

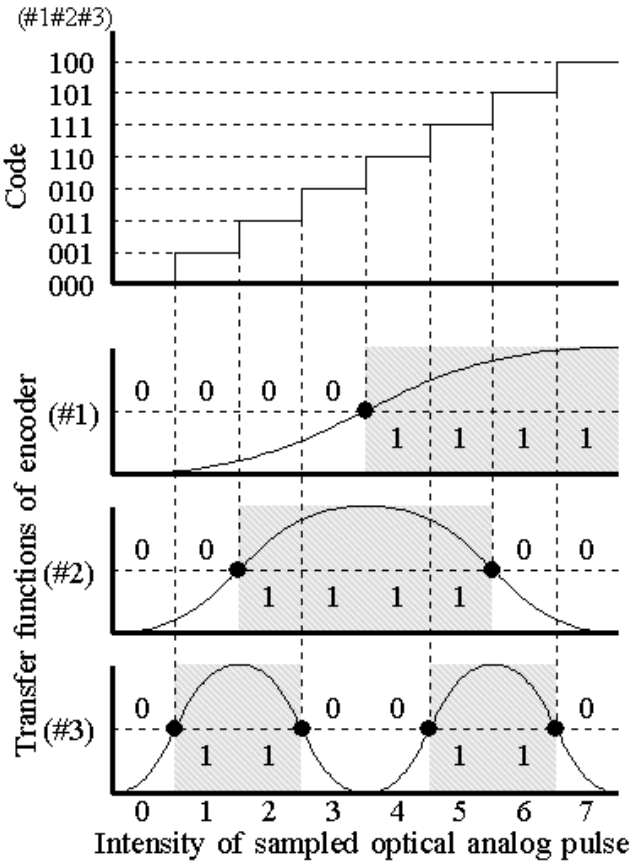

Fig. 2.2 Transfer functions of the encoders for 3-bit A/D conversion with Gray code.

2.3 Nonlinear Optical Loop Mirror (NOLM)

Each encoder consists of a nonlinear optical loop mirror (NOLM), and its configuration is shown in Fig. 2.3. The NOLM consists of a 3-dB coupler, a WDM coupler, a band pass filter (BPF), a highly non-linear fiber (HNLF), and polarization controllers (PCs). The sampled optical analog signals operating at λ_1 are launched into $Input_1$ port as control pulses. The probe pulses operating at λ_2 are synchronized with the optical analog pulses and are inputted into $Input_2$ port. A probe pulse is divided into clockwise and counter-clockwise traveling pulses by the 3dB-coupler. The pulses traveling clockwise receive cross-phase modulation from the co-traveling split control pulses. The phase shift $\phi_{XPM\text{-}CW}$ due to this cross phase modulation (XPM) is given approximately by

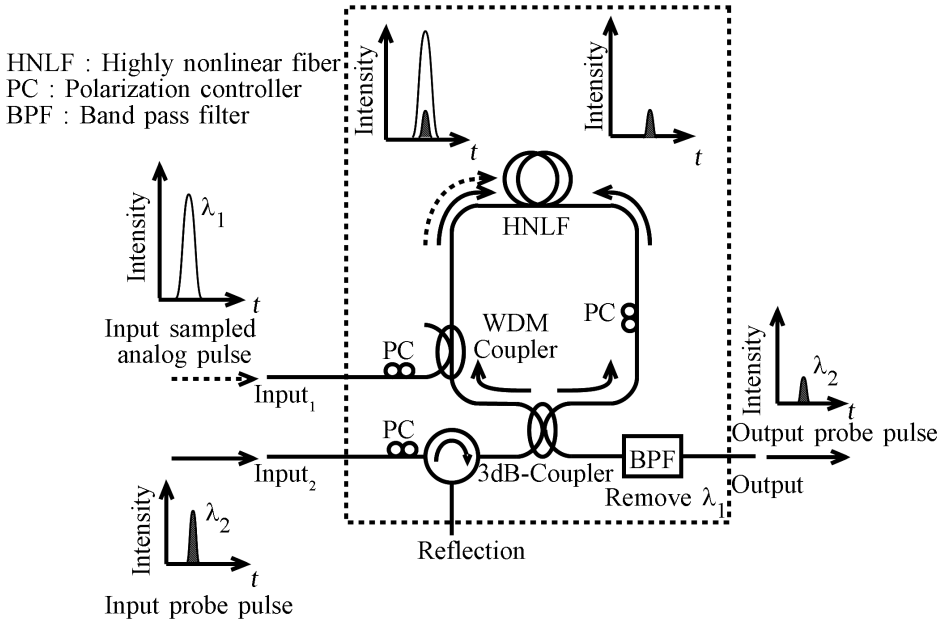

Fig. 2.3 Configuration of nonlinear optical loop mirror for the encoder.

$$\phi_{XPM-CW} = 2\gamma P_{peak} L, \tag{2.1}$$

where γ and L are the nonlinear coefficient and length of the highly non-linear fiber (HNLF), respectively. P_{peak} is the peak power of the control pulse. This phase shift ϕ_{XPM-CW} is used for the switching operation of the NOLM.

On the other hand, the control pulses induce unwanted phase shift, which is not desired for the switching on the counter-clockwise traveling probe pulses at the same time. The counter-clockwise traveling probe pulses receive the phase shift when the control pulses pass through them in the HNLF. The phase shift $\phi_{XPM-CCW}$ of the counter-clockwise traveling probe pulse is given by the average power of the control pulses as,

$$\begin{aligned} \phi_{XPM-CCW} &= 2\gamma P_{ave}(t) L \\ &= \frac{\gamma L}{\tau} \int_{t-\tau}^{t+\tau} P(t')dt', \end{aligned} \tag{2.2}$$

where t is the time when the probe pulse is input into the HNLF. $P_{ave}(t)$ is the average power of control pulses in the HNLF, which may be taken as time-dependent in practical applications. τ is the transit time of the probe pulse in the HNLF, and $P(t)$ is the power of input control pulses into the HNLF. We note that P_{ave} is a time-varying function, whose response time is comparable with

the transit time 2τ. The electric fields E_{CW}, E_{CCW} of clockwise and counter-clockwise traveling probe pulse after passing through the HNLF are given by

$$E_{CW} = \frac{1}{\sqrt{2}} E_0 \exp(i\phi_{XPM-CW}), \tag{2.3}$$

$$E_{CCW} = \frac{i}{\sqrt{2}} E_0 \exp(i\phi_{XPM-CCW}), \tag{2.4}$$

respectively, where E_0 is input electric field of the probe pulse. The electric field of the output probe pulse E_{OUT} is given by

$$\begin{aligned} E_{OUT} &= \frac{1}{\sqrt{2}} \bullet \frac{1}{\sqrt{2}} E_0 \exp(i\phi_{XPM-CW}) \\ &+ \frac{i}{\sqrt{2}} \bullet \frac{i}{\sqrt{2}} E_0 \exp(i\phi_{XPM-CCW}) \\ &= \frac{E_0}{2} \left[\exp(i\phi_{XPM-CW}) - \exp(i\phi_{XPM-CCW}) \right] \end{aligned} \tag{2.5}$$

The output power P_{OUT} is given by

$$P_{OUT} = \frac{1}{2} P_{IN} \left\{ 1 - \cos\left(\Delta\phi_{XPM} \right) \right\}, \tag{2.6}$$

where P_{IN} is the power of the input probe pulse, $\Delta\phi_{XPM}$ is the phase difference between the clockwise and counter-clockwise probe pulses and can be calculated from Eqs. (2.1), (2.2), and (2.6) as

$$\begin{aligned} \Delta\phi_{XPM} &= \phi_{XPM-CW} - \phi_{XPM-CCW} \\ &= 2\gamma P_{peak} L - 2\gamma P_{ave}(t) L \\ &= \gamma L \left(2P_{peak} - \frac{1}{\tau} \int_{t-\tau}^{t+\tau} P(t')dt' \right). \end{aligned} \tag{2.7}$$

It should be noted that P_{OUT} depends on $\phi_{XPM\text{-}CCW}$, which is time-varying. This phenomenon is

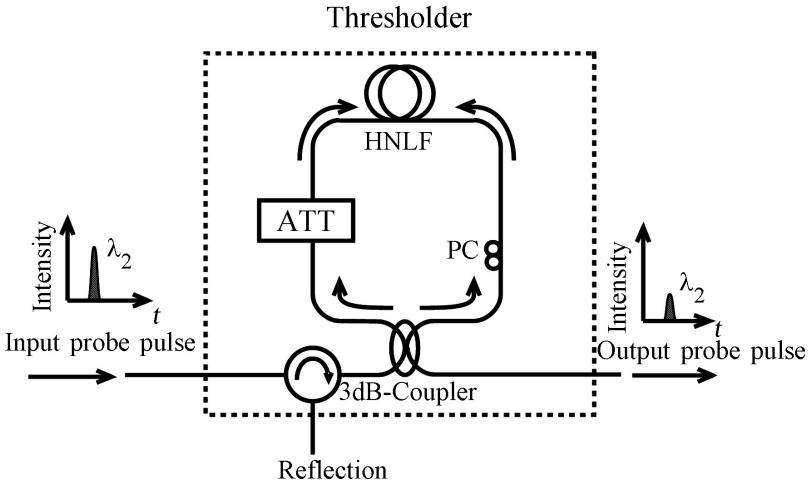

Fig. 2.4 Configuration of nonlinear optical loop mirror for the encoder

called counter-propagating effect [23]. Because the NOLM we have used approximately 400-m-long HNLF, more than tens of thousand of control pulses are included in the transit time 2τ, at the sampling rate of 10 GS/s. Therefore, the $\phi_{XPM\text{-}CCW}$ can be regarded as almost constant as fast varying analog signal is assumed. If the HNLF in the NOLM is a non-polarization-maintaining HNLF, this effect can be compensated by the polarization controller of the NOLM [30]. For a NOLM using a polarization-maintaining HNLF, solutions using an optical bias controller or optical phase-bias compensator (OPBC) have been studied [31, 32]. The design considerations have to carefully include the issues associated with this phenomenon. Here, we neglect the fiber loss, changes in pulse shape and polarization, and walk off due to the fiber dispersion to simplify the discussion.

Figure 2.5 shows a thresholder using a NOLM, which is consist of a circulator a 3-dB coupler , a HNLF, a PC, and attenuator (ATT). The quantities of SPM for the clockwise pulses $\phi_{SPM\text{-}CW}$ and counter-clocwise traveling pulses $\phi_{SPM\text{-}CCW}$ can be written by equations

$$\phi_{SPM-CW} = \alpha \frac{P_{IN-th}}{2} \gamma L, \tag{2.8}$$

$$\phi_{SPM-CCW} = \frac{P_{IN-th}}{2} \gamma L, \tag{2.9}$$

respectively, where $P_{IN\text{-}th}$ and α are the input power of the probe pulse and the loss due to the ATT

in the loop, respectively. Here, we neglect the counter-propagating effect to simplify the discussion. The electric fields $E_{CW\text{-}th}$, $E_{CCW\text{-}th}$ of clockwise and counter-clockwise traveling probe pulse after passing through the HNLF and ATT are given by

$$E_{CW-th} = \sqrt{\frac{\alpha}{2}} E_{probe-th} \exp(i\phi_{SPM-CW}), \tag{2.10}$$

$$E_{CCW-th} = i\sqrt{\frac{\alpha}{2}} E_{probe-th} \exp(i\phi_{SPM-CCW}), \tag{2.11}$$

respectively, where $E_{probe\text{-}th}$ is input electric field of the probe pulse. The electric field of the output probe pulse $E_{OUT\text{-}th}$ is given by

$$\begin{aligned} E_{OUT-th} &= \frac{1}{\sqrt{2}} \bullet \sqrt{\frac{\alpha}{2}} E_{probe-th} \exp(i\phi_{SPM-CW}) \\ &+ \frac{i}{\sqrt{2}} \bullet i\sqrt{\frac{\alpha}{2}} E_{probe-th} \exp(i\phi_{SPM-CCW}) \\ &= \frac{E_{probe-th}}{2}\sqrt{\alpha}\left[\exp(i\phi_{SPM-CW}) - \exp(i\phi_{SPM-CCW})\right] \end{aligned} \tag{2.12}$$

The output power $P_{OUT\text{-}th}$ of the thresholder is given by

$$\begin{aligned} P_{OUT-th} &= \frac{1}{2}\alpha P_{IN-th}\left\{1 - \cos(\phi_{SPM-CW} - \phi_{SPM-CCW})\right\} \\ &= \frac{1}{2}\alpha P_{IN-th}\left[1 - \cos\left\{\frac{(1-\alpha)\gamma L}{2} P_{IN-th}\right\}\right]. \end{aligned} \tag{2.13}$$

The transfer function can be used as thresholder, which suppresses “0” level signals and tailors “1” level signals.

2.4 Design Considerations of Multi-Period NOLM

In section 2.3, we neglected the fiber loss, changes of pulse shape, and walk-off due to the fiber dispersion. In this section, effects due to the fiber nonlinearity and group velocity dispersion (GVD)

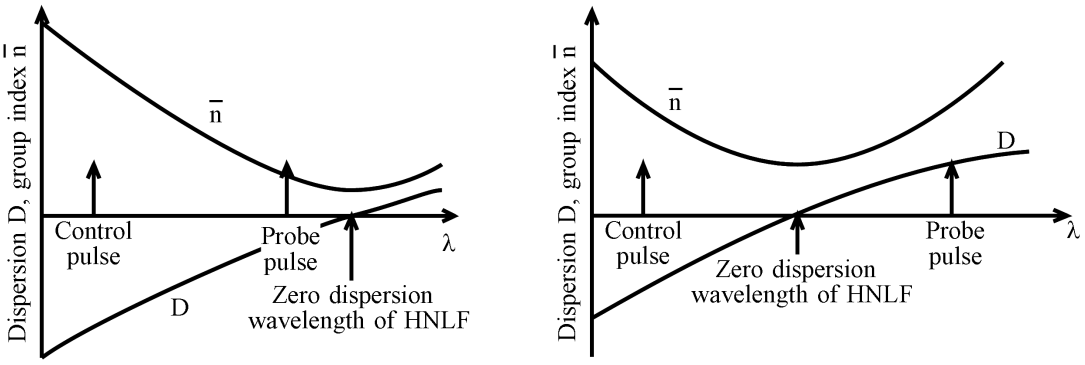

(a) Design 1. (b) Design 2.

Fig. 2.5 Wavelength allocation design.

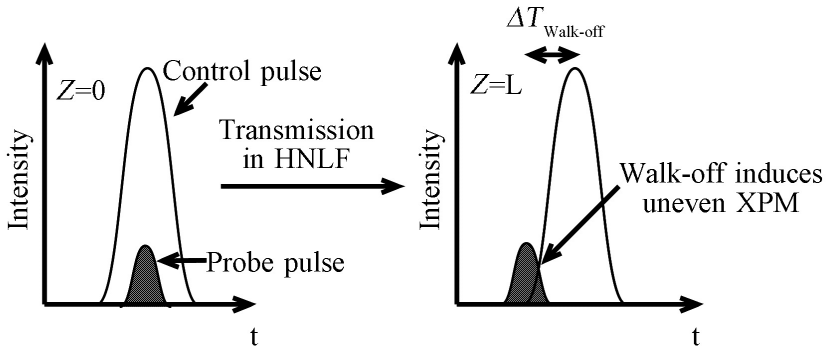

Fig. 2.6 Uneven XPM by walk-off.

are discussed. To realize multi-period transfer functions in a NOLM, the cross-phase modulation of the probe pulse travelling clockwise at λ_P by a high-intensity control pulse at λ_C has to be maximized by mitigating walk-off through a careful design of the wavelength allocation of λ_P and λ_C by taking into account of the group velocity dispersion (GVD). The wavelength allocation of the control and probe pulses has to be optimized with respect to the chromatic dispersion of highly nonlinear fiber (HNLF). In the past, to reduce parametric gain, and to avoid unwanted soliton phenomena the wavelengths of both control and probe pulses be placed normal dispersion region, as shown in Fig 2.5 (a). However, this wavelength allocation induces the walk-off problem, which is caused by the difference of group velocity between the control pulse and probe pulse. The walk-off reduces the XPM efficiency and the extinction ratio of transfer function, because the control pulse can't induce uniform phase shift to the whole clockwise traveling probe pulse by walk-off and fiber loss, as shown in Fig. 2.6. The uneven phase shift broadens a spectrum of the probe pulse. Such a clockwise traveling probe pulse cannot fully interfere with counter-clockwise traveling probe pulse. The differential transit time $\Delta T_{walk\text{-}off}$ between the control pulse and probe pulse can be written as

$$\Delta T_{walk-off} = DL\left(\lambda_{control} - \lambda_{probe}\right), \tag{2.5}$$

where D and L are the dispersion and fiber length of HNLF in the NOLM, respectively. $\lambda_{control}$ and λ_{probe} are wavelengths of the control and probe pulse.

To minimize walk-off, the wavelength interval between control pulse and probe pulse, and the dispersion parameter should be minimized. However, if both the dispersion parameter and differential wavelength interval are too small, the transfer function profile will be deformed because the probe pulses travelling clockwise are amplified by parametric gain, depending on the power of the control pulse. The parametric amplification gain G can be written as [15]

$$G = 1 + (2\gamma P_{control} / g)^2 \sinh^2(gz), \tag{2.6}$$

$$g = \sqrt{(2\gamma P_{control})^2 - (\kappa/2)^2}, \tag{2.7}$$

$$\kappa = \Delta k + 2\gamma P_{control}, \tag{2.8}$$

where L, γ are the fiber length and the nonlinear coefficient of a HNLF in a NOLM. $P_{control}$ is the power of a control pulse. κ, g and Δk are, the net phase mismatch, the parametric gain, and the phase mismatch. In order to reduce the amplification factor, the phase mismatch Δk should be increased by increasing the difference of the control pulse wavelength and the probe pulse wavelength, and increasing the difference of the control pulse wavelength and the zero dispersion wavelength.

Fig. 2.5 (b) shows the wavelength allocation to suppress both influences of walk-off and the parametric amplification. In this allocation, the wavelength of the control pulse is located in normal dispersion region. On the other hand, the wavelength of the probe pulse is located in the anomalous dispersion region, which is symmetric to that of the control pulse with respect to the zero dispersion wavelength. It is possible to achieve the same group velocity between control pulse and probe pulse [7]. If the wavelength interval between the control pulse and the probe pulse is large enough, this allocation will be available not only to suppress parametric amplification but also to suppress walk-off.

At the same time, the spectral broadening of the control pulse caused by self-phase-modulation (SPM) and Raman effect has to be taken into account. If the wavelength spacing between the control and probe pulse is too narrow, the broadened spectrum of the control pulse overlaps with the probe pulse. The overlapped control pulse cannot be removed at output port by band pass filter.

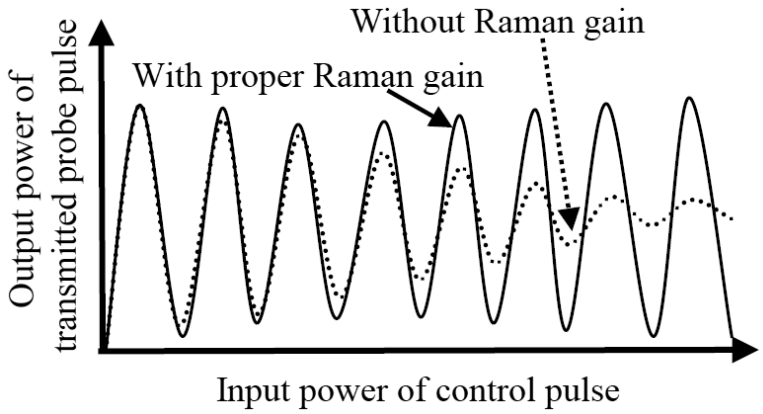

Fig. 2.7 Effect of Raman gain on transfer function of multi-period NOLM.

If the wavelength spacing is too wide, the power of probe pulse travelling clockwise is Raman-amplified by the control pulse. The Raman gain increases as the wavelength spacing approaches to 100 nm [15]. Too high gain degrades the transfer function. However, a proper gain improves transfer function profile, because the gain compensates the decreased power of probe pulse due to spectrum broaden by uneven XPM and filtering by BPF, as shown in Fig. 2.7.

2.5 Numerical Simulations and Demonstrations

2.5.1 Design Comparison of NOLMs

In this section, we compare designs by numerical simulation. Figure 2.8 shows the simulation model of the NOLM. In order to consider both the effects of uneven XPM and Raman amplifier in HNLF, we used the split-step Fourier method [15]. However, the pulses transmitted bi-directionally cannot be simulated by this method. So we split the counter-clockwise and clockwise paths into two different paths. The control pulse and the probe pulse are input to the upper side path as the clockwise path from the WDM coupler and the 3-dB coupler. To the lower side path, only probe pulse is input as counter-clockwise path from 3-dB coupler. It is assumed that control and probe pulse maintain the same polarization state. Figure 2.9 and Table 2.1 show the group delay, the dispersion of HNLF, the wavelength allocation, and the parameters of each design. The zero dispersion wavelength, the dispersion slope, the nonlinear coefficient, and the length of HNLF are assumed to be $\lambda_0 = 1567.7$ nm, Ds = 0.02 ps/km^{-1}nm^{-1}, $\gamma = 9.0$ W^{-1}km^{-1}, and L = 403 m, respectively.

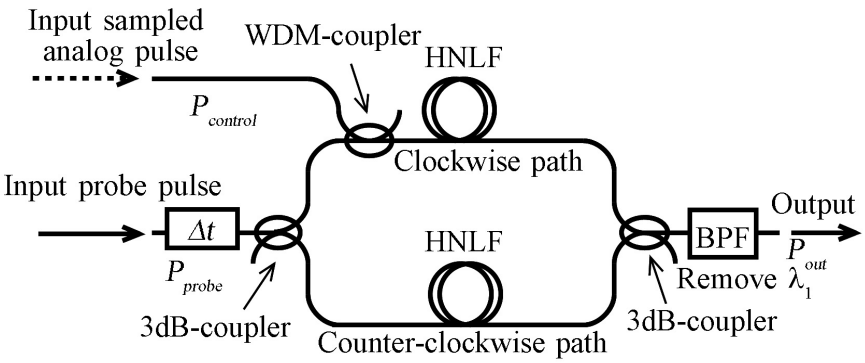

Fig. 2.8 Simulation model of the NOLM.

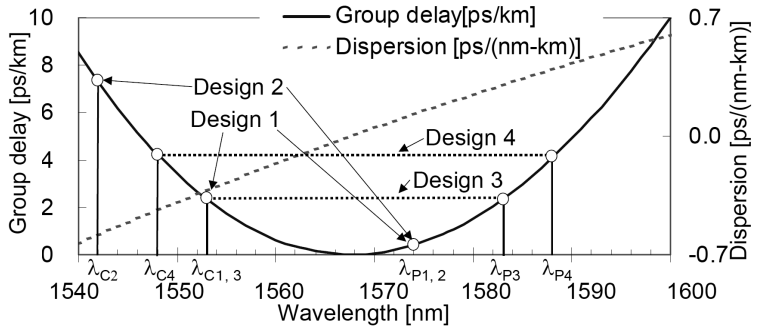

Fig. 2.9 HNLF parameter and Designs of wavelength allocation.

Table 2.1 Parameters of Designs.

	Control pulse		Probe pulse		Walk-off
	λ_C [nm]	T_C [ps]	λ_P [nm]	T_P [ps]	T_W [ps]
Design 1a	1553.0	4.11	1572.0	1.22	0.868
Design 1b	1553.0	2.58	1572.0	1.19	0.868
Design 2	1542.0	2.04	1572.0	1.34	2.870
Design 3	1553.0	2.04	1583.0	1.34	0.002
Design 4	1548.2	2.04	1588.2	1.34	0.004

The walk-off is more suppressed in Designs 3 and 4 than Design 1 and 2. The wavelength spacings between the control and probe pulses in Designs 2, 3 and 4 are 30 nm, 30 nm, and 40 nm, respectively. In Designs 1b, 2, 3, 4 and 5 the pulse width of the control pulse T_C and probe pulse T_P are approximately 2 ps and 1 ps, respectively, because the A/D converter is targeted for the sampling rate above 100-GS/s. Figure 2.9 shows the simulation results of the transfer functions of

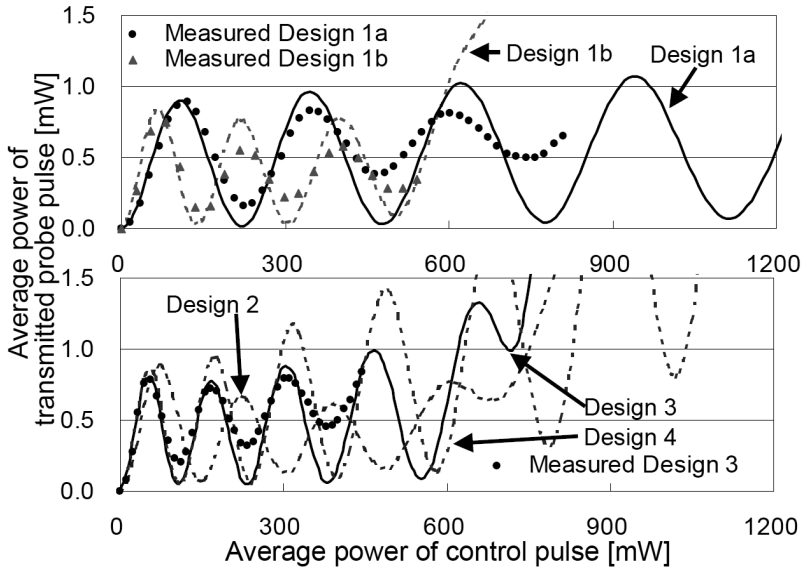

Fig. 2.10 Numerical (line) and experimental (plot) power transfer function of NOLM.

the NOLM with the five designs. The transfer function of Design 1a achieves 4 periods. However in Design 1b the transfer function cannot achieve 4 periods, because the broadened spectrum of the control pulse overlaps with the probe pulse at an average power of 550 mW. The wavelength spacing, 19 nm, is too narrow for the pulse width of 2.58 ps. The extinction ratio in Design 2 is lower than the one in Design 3, due to the large walk-off (2.87 ps), while those of Designs 3, and 4 are improved due to smaller walk-off. The transfer functions of Designs 3 and 4 achieve 4 periods. However, the effect of Raman amplification is large in Design 4. Overall, Design 3 is the optimum for 4-bit A/D conversion in these Designs. To support this Design consideration, we experimentally demonstrated Designs 1a, 1b and 3.

Figure 2.11 shows the experimental setup to measure the transfer function of the NOLM. The control and probe pulse parameters, and fibre parameters of $HNLF_2$ were substantially the same as the simulation parameters of Design 1a, 1b, and 3, respectively. We note that in Designs 1a and 1b, a different HNLF was used; the wavelengths of control and probe pulse, and the zero dispersion wavelength were shifted by -2 nm. Because the dispersion slopes of the HNLFs used were the same, the conditions were theoretically equivalent to those listed in Table 2.1. The sampling rate was 40-GS/s but the pulse width was approximately 2 ps so that sampling rate higher than 100-GS/s could be demonstrated in Design 1a and 3. To generate the probe pulse train, we used a 40-GHz pulse source consisting of a tuneable laser source (TLS) operating at 1583 nm or 1570 nm depending on the condition, a RF oscillator, a LN intensity modulator, an EDFA and a pulse compressor so-called comb-like profiled fibre (CPF) [34]. We generated control pulses from the wavelength conversion of the probe pulses in $HNLF_1$ through the degenerate four-wave mixing

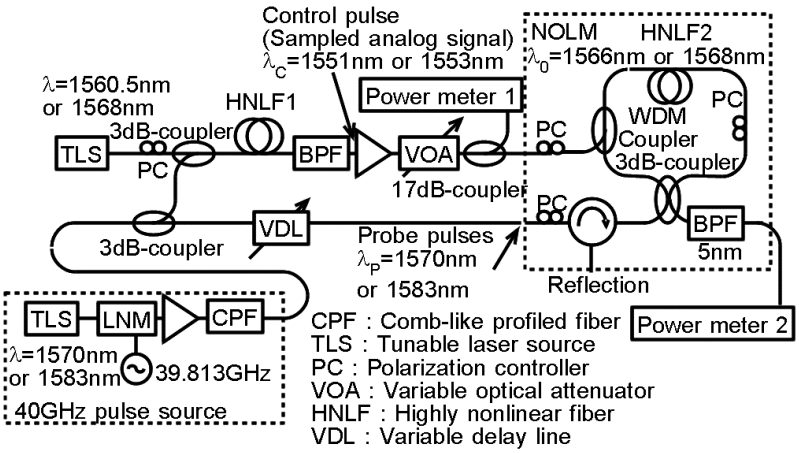

Fig. 2.11 Experimental setup.

with the continuous wave pump light at 1568 nm or 1560.5 nm. The pulse width of the control pulses was adjusted by the bandwidth of a band pass filter (BPF). A variable optical attenuator (VOA) was used to emulate level change of the optical analog signal input. The variable delay line (VDL) was adjusted so as to overlap the probe pulse with the control pulse. Two PCs at each input adjusted the polarization states of the control and probe pulses to be matched efficiently for inducing XPM. In this experiment, we could measure nearly 4-period sinusoidal transfer function. However, compared with the simulation results, the input power required for Designs 1a, 1b, and 3 in the experiment was larger by factors of 1.16, 1.18, and 1.41, respectively. The difference presumably arises from the misalignment of the polarization states due to indefinitely varying birefringence of the HNLF. Therefore, as a fair comparison, we modify the powers of control pulse by these factors, and co-plot the modified measured transfer function of the NOLM in Fig. 2.10. We find from Fig. 2.10 that the extinction ratio of the experimental transfer functions is worse than the simulated ones. One plausible reason is due to the timing fluctuation between the control and probe pulse during measurement. We speculate that it should be solved by stabilizing the timing.

2.5.2 Demonstration of multi-period transfer function

Figure 2.11 shows the experimental setup to measure multi-period transfer function of NOLM. This experimental setup was solved above the timing fluctuation problem by using a timing stabilizer. For the control pulses, or the sampled analog pulses, we used a 10-GHz mode-locked fiber ring laser (FRL) operating at a wavelength of 1542 nm. To generate high power control

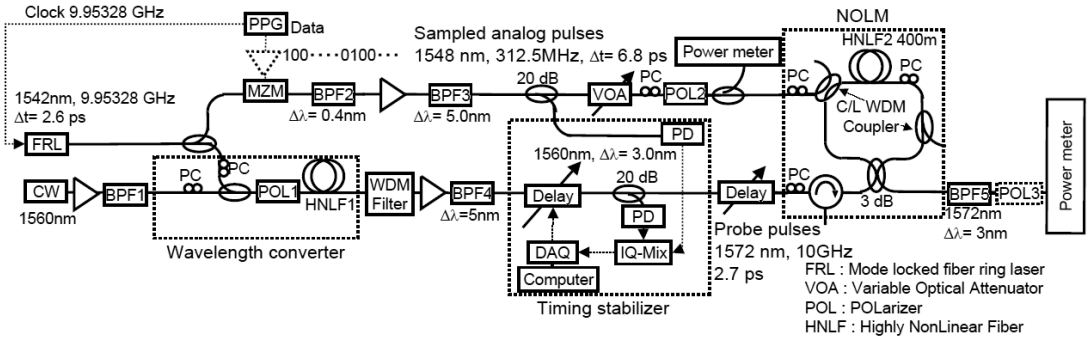

Fig. 2.12 Experimental setup for demonstration of multi-period transfer function of NOLM.

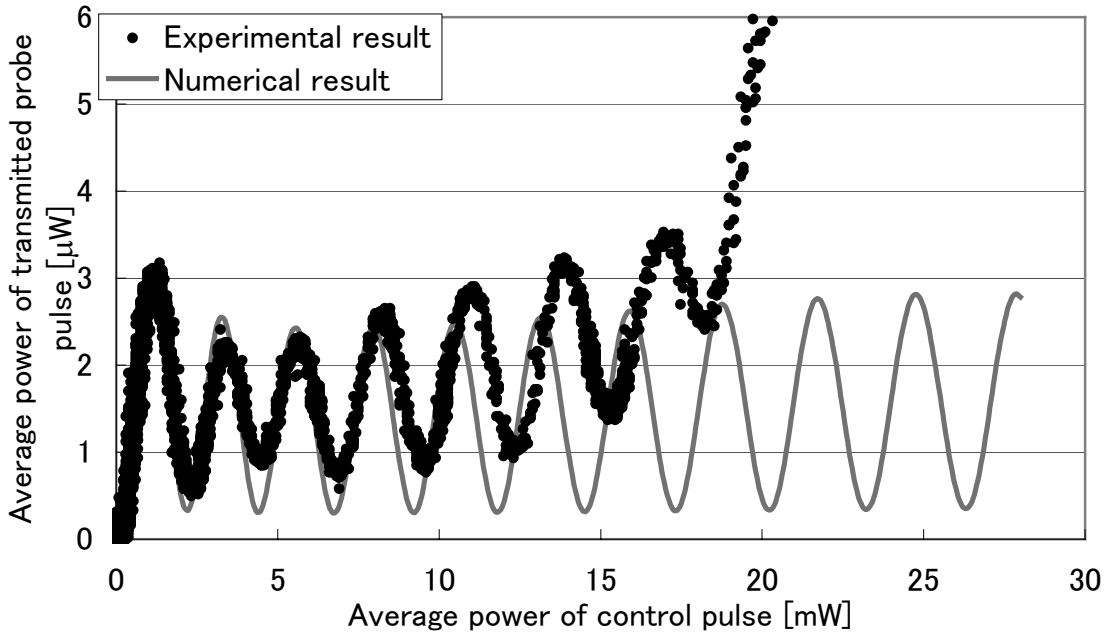

Fig. 2.13 Numerical and Experimental results.

pulses, the repetition rate of control pulses were decreased by a Mach Zehnder modulator (MZM). We generated the probe pulses by means of the wavelength conversion of the control pulses through four-wave mixing (FWM) in $HNLF_1$ with a tunable laser source (TLS) whose wavelength is set at 1560 nm. The probe pulses, which were generated at a wavelength of 1572 nm with a pulse width of 2.7 ps, were synchronized with the control pulses. The BPF_2 with a 3-dB bandwidth of 0.4 nm was used to expand the pulse width of the control pulses up to 6.8 ps. A variable optical attenuator (VOA) was used to emulate the changing levels of the optical analog signal input. A variable delay line (VDL) was set so as to overlap the probe pulse train with the control pulses. The zero dispersion wavelength, the dispersion slope, the nonlinear coefficient, and the length of the

HNLF are assumed to be λ_0 = 1560 nm, Ds = 0.02 ps/km-nm^2, γ = 12.0 1/W-km, and L = 400 m, respectively. Two PCs at each input adjusted the polarization states of the control and the probe pulses to be matched efficiently for inducing XPM. The PC in the loop is used in order to adjust the bias setting so that all probe pulses are output to the reflection port, when the control pulses are absent. The BPF_5 placed at the output of the NOLM removes the control pulses and only transmits the probe pulses. Figure 2.13 is the numerical and experimental result, which shows the nearly 8-period transfer function of the NOLM. This discrepancy between numerical and experimental results is probably due to the mismatching of the polarization states between the control pulses and the probe pulses in the $HNLF_2$. The mismatching cannot be inevitable by only adjusting the PCs, because the control and probe pulses are received wavelength-dependent polarization rotations from indefinitely varying birefringence of the HNLF. The polarization mismatch decreases the efficient of XPM, and the extinction ratio due to the nonlinear polarization rotation, which depends on the intensity of sampled analog signals. In future, a 5-bit A/D conversion will be possible by completely matching the polarization states of the control pulses and the probe pulses using a polarization-maintaining HNLF.

2.6 Conclusion

In this chapter, an optical quantizing and coding scheme using multi-period transfer functions were introduced. We investigated numerical design considerations of a NOLM that had been confirmed by experiment, and consequently demonstrated a record, nearly 4-period transfer function for a control pulse width of approximately 2 ps capable of 4-bit A/D conversion at the sampling rate of 100-GS/s. Finally we demonstrated nearly 8-period transfer function of NOLM. In future, the 5-bit A/D conversion will be possible using a polarization-maintaining HNLF.

Chapter 3

All-optical Quantizing and Coding Using Split-and-Delay Technique

3.1 Introduction

In this chapter, we propose an all-optical quantizing and coding scheme using a split-and-delay technique. The Split-and-delay technique simplifies the configuration of the A/D converter and supports a high-resolution all-optical A/D converter. The conventional all-optical A/D conversion scheme, which is introduced in Chapter 2 required N-encoders, and N-thresholders for N-bit optical quantizing and optical coding. Therefore, the problems of size, complexity and polarization instability become conspicuous when the resolution is high. The A/D converter using the split-and-delay technique requires only one encoder and one thresholder for N-bit A/D conversion. This technique can change the sample rate and the resolution only by changing the operation of the sampler and the split-and-delay coupler (SDC), and thus the convenience of the all-optical A/D converter increases.

3.2 Split-and-Delay Technique

In the scheme of conventional A/D conversion, which was described in Section 2.3, in order to increase resolution, the number of encoders and thresholders had to be increased. In conventional scheme, N-encoders with a different periodical transfer function for each bit were required for N-bit A/D conversion. Therefore, the problems of size and complexity become conspicuous when the resolution is high. On the other hand, the configuration of proposal scheme dose not become complex even at high resolution A/D conversion, because the A/D converter using split-and-delay technique requires only one encoder and one thresholder even at N-bit A/D conversion. Figure 3.1 schematizes this process for 3-bit A/D conversion. As shown on the right-hand side of Fig. 3.1, in order to realize the coding based on Gray code, the 3-bit A/D converter needs to have the periodic transfer functions with three different periods. The transfer function of #N requires 2^{N-2} periods for N-bit A/D conversion. The intensity of the output pulse for each bit of #1, #2, and #3 takes a value either "0" or "1", depending on the intensity of an optical analog pulse. For example, when the intensity of an input analog signal is "6", the output pulses of #1, #2 and #3 encoder are "1", "0" and "1", respectively. This scheme requires N-encoders for N-bit A/D conversion.

The block diagram of our proposed all-optical quantization and coding for N-bit A/D conversion using a novel split-and-delay technique is shown in Fig. 3.2(a). The A/D converter consists of a split-and-delay coupler (SDC), an encoder and a thresholder. The SDC splits a sampled optical analog pulse into N analog pulse trains with a set of pre-determined splitting ratios. Their delay

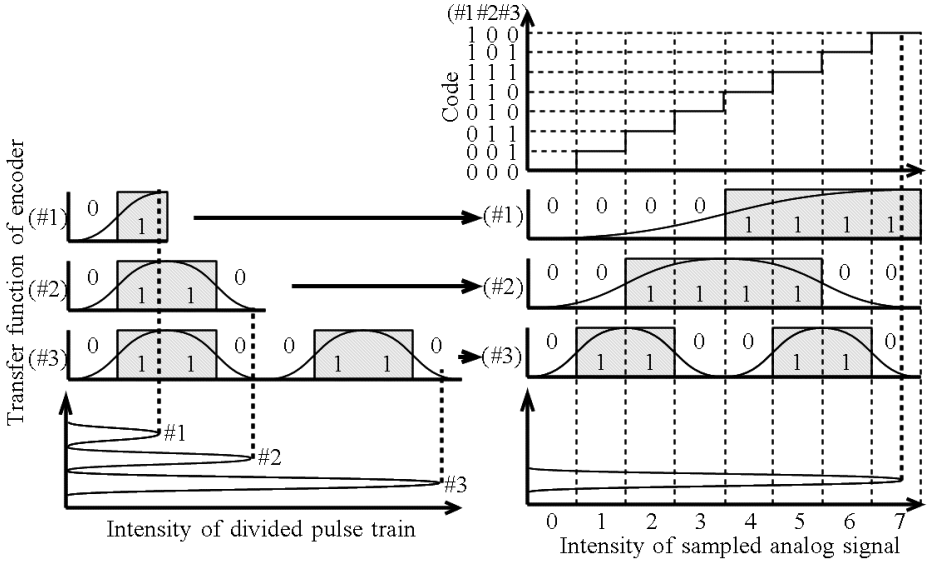

Fig. 3.1. Gray code and transfer function of the encoders and split-and-delay technique.

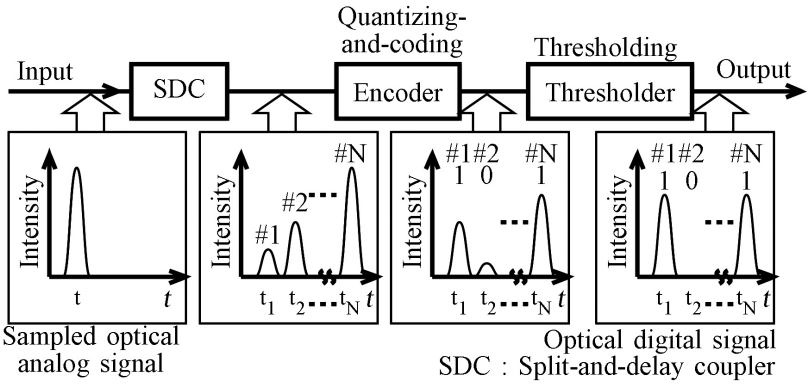

(a) Proposed scheme using split-and-delay technique.

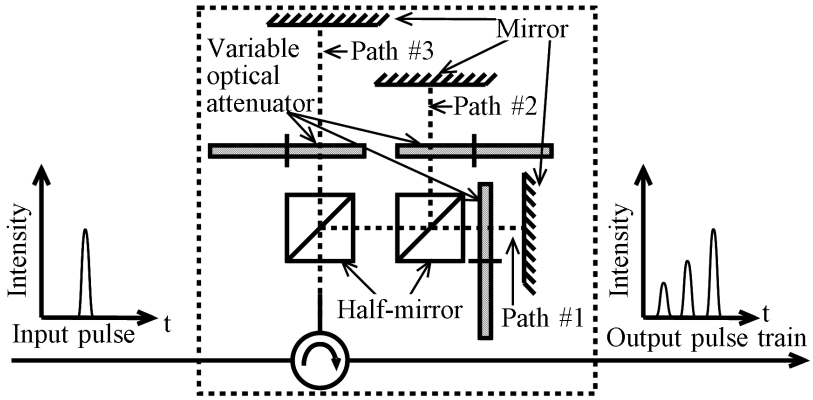

(b) Configuration of split-and-delay coupler for 3-bit A/D conversion.

Fig. 3.2 Split-and-delay technique.

interval is determined by the target sampling resolution N. The encoder and the thresholder have the operation speed of N-times the sampling speed. An example of 3-bit quantization and coding is shown on the left-hand side of Fig. 3.1. If the relative power ratios for the split and delayed pulses were set $1/2^2$, $1/2^1$, and $1/2^0$, respectively, then one encoder could provide effectively a different period for each of the split pulses. Namely, in the case of Fig. 3.1, the encoder exhibits different transfer functions; (#1) half-, (#2) single- and (#3) two-period transfer function in each time-slot, respectively, for one input analog pulse.

The configuration of a SDC for the 3-bit A/D conversion is shown in Fig. 3.2(b). This SDC consists of two half mirrors, three mirrors, three variable optical attenuators, and an optical circulator. The input pulse is split into three pulses by the half mirrors, and the split pulses are reflected back and coupled together again. The delays and relative power ratios of three divided pulses are given by the difference of their path lengths and the variable optical attenuators, respectively. It is noteworthy that this technique allows us to increase the intensity resolution of A/D conversion by sacrificing the

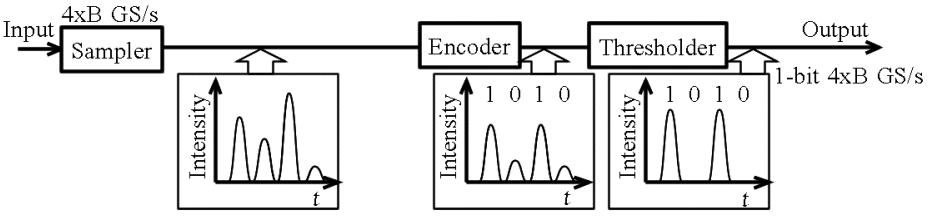

(a) 1-bit A/D conversion at sampling late of 4xB GS/s.

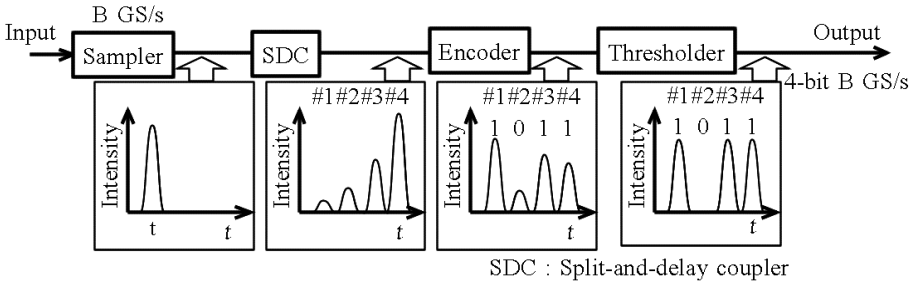

(b) 4-bit A/D conversion sampling late of B GS/s.

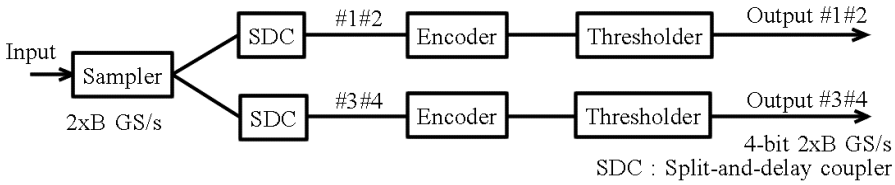

(c) Hybrid approach to 4-bit A/D conversion sampling late of 2xB GS/s.

Fig. 3.3 Variable sampling rate and resolution.

temporal resolution. In other words, the use of this split-and-delay technique is indeed to exploit the bandwidth of the encoder for increasing the number of bits, as is exemplified in Fig. 3.3. In Fig. 3.3(a), the sampler can operate at a sampling rate of 4xB GS/s, when the split-and-delay technique is not used. The encoder and thresholder operate for 1-bit A/D conversion at 4xB GS/s. If we employ the split-and-delay technique, the sampling rate can be changed to B GS/s, and the sampled analog pulse divides into 4 pulses by a SDC as shown in Fig. 3.3(b). The encoder then realizes the half-, single- two- and four- period transfer function at time-slots #1, #2, #3, and #4 respectively. As a result, the encoder and thresholder can operate as a 4-bit A/D converter at a sampling rate of B GS/s, while the encoder operates at the same clock frequency of 4xB GHz. Thus, the temporal resolution is utilized to increase the intensity resolution. If two split-and-delay units were operated in parallel, 4-bits at 2xB GS/s would be realized. This is so called hybrid approach to obtain both high-resolution and high-speed. And the split-and-delay technique allows us to save the number of encoders, leading to a much simpler configuration compared to the conventional setup.

3.3 Principle Operation of Encoder Using Split-and-Delay Technique

The encoder we use here is a NOLM with the configuration as shown in Fig. 3.4. While SDC_1 divides a sampled analog pulse operating at λ_1 into N control pulses with the designated splitting ratios, SDC_2 divides a probe pulse operating at λ_2 into N probe pulses with an equal intensity. The divided probe pulse train is synchronized with the optical analog pulses.

When the probe pulses enter the NOLM, they split into the two directions; one is clockwise and the other is counter-clockwise. The clockwise traveling pulses receive cross-phase modulation from the co-traveling split control pulses. The phase shift $\phi_{XPM\text{-}CWi}$ (i=1, 2, … N) due to this cross phase modulation (XPM) is given approximately by

$$\phi_{XPM-CWi} = 2\gamma P_{peaki} L, \tag{3.1}$$

where γ and L are the nonlinear coefficient and length of the highly non-linear fiber (HNLF), respectively. P_{peaki} is the *i*-th peak power of the control pulse overlapped with the probe pulse in each time-slot. This phase shift $\phi_{XPM\text{-}CWi}$ is used for the switching operation of the NOLM.

However, the control pulses induce unwanted phase shift on counter-clockwise traveling probe pulses at the same time. The counter-clockwise traveling probe pulses receive the phase shift when the control pulses pass through them in the HNLF. The phase shift $\phi_{XPM\text{-}CCW}$ of the counter-clockwise traveling probe pulse is given by the average power of the control pulses as,

$$\begin{aligned}\phi_{XPM-CCW} &= 2\gamma P_{ave}(t) L \\ &= \frac{\gamma L}{\tau}\int_{t-\tau}^{t+\tau} P(t')dt',\end{aligned} \tag{3.2}$$

where t is the time when the probe pulse is input into the HNLF. $P_{ave}(t)$ is the average power of control pulses in the HNLF, which may be taken as time-dependent in practical applications. τ is the transit time of the probe pulse in the HNLF, and $P(t)$ is the power of the input control pulses into the HNLF. We note that P_{ave} is a time-varying function, whose response time is comparable with the transit time 2τ. The output power P_{OUTi} of the *i*-th time-slot is given by

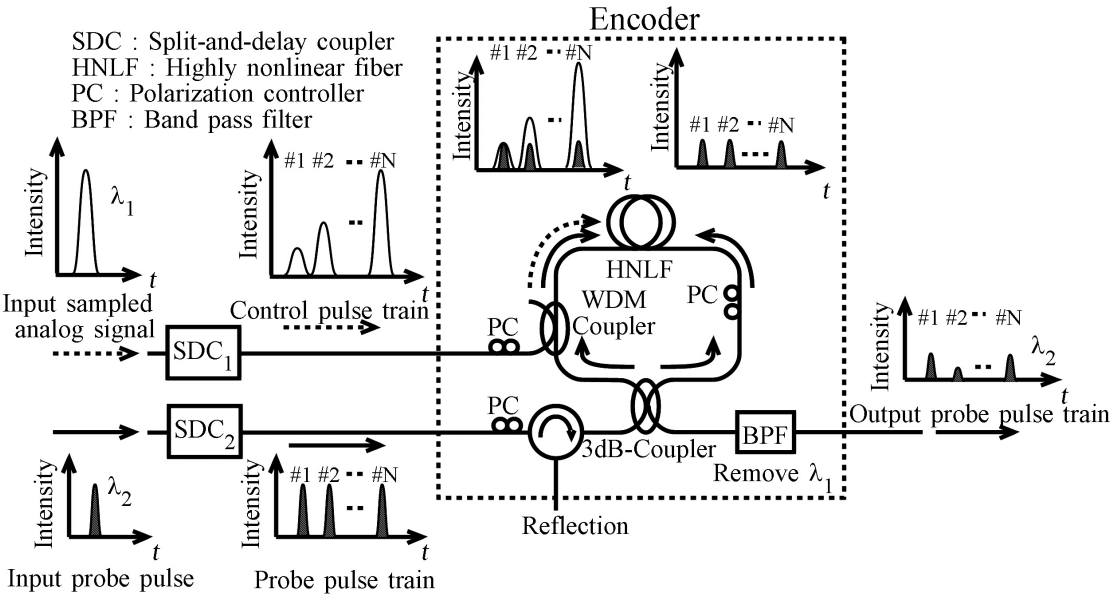

Fig. 3.4 Configuration of the encoder.

$$P_{OUTi} = \frac{1}{2} P_{INi} \{1 - \cos(\Delta\phi_{XPMi})\}, \tag{3.3}$$

where P_{INi} is the power of the input probe pulse, the subscript i denotes the i-th time slot, and $\Delta\phi_{XPMi}$ is the phase difference between clockwise and counter-clockwise probe pulses and can be calculated from Eqs. (3.1), (3.2), and (3.3) as

$$\begin{aligned} \Delta\phi_{XPMi} &= \phi_{XPM-CWi} - \phi_{XPM-CCW} \\ &= 2\gamma P_{peaki} L - 2\gamma P_{ave}(t) L \\ &= \gamma L \left(2P_{peaki} - \frac{1}{\tau} \int_{t-\tau}^{t+\tau} P(t) dt \right). \end{aligned} \tag{3.4}$$

It should be noted that P_{OUTi} depends on $\phi_{XPM\text{-}CCW}$ which is time-varying. This phenomenon is called counter-propagating effect [31]. The design considerations have to carefully include the issues associated with this phenomenon.

3.4 Counter-Propagating Effect in Sprit-and-Delay Technique

Let us estimate the SDC power splitting ratios, accounting for different regimes of the counter-propagating effects. The encoder needs to have the (#1) half-, (#2) single- and (#3) two-period transfer function for the input analog pulse in each time-slot for 3-bit quantizing and coding. Then, the phase shift ratio of $\Delta\phi_{XPMi}$ has to be set so as to satisfy the following equation.

$$\Delta\phi_{XPM1} : \Delta\phi_{XPM2} : \cdots : \Delta\phi_{XPMN} = 1 : 2 : \cdots : 2^{N-1}. \tag{3.5}$$

3.4.1 Characteristics of the Encoder without Counter Propagating Effect

The first regime we consider is the case where the average power of the control pulses P_{ave} is enough small compared with their peak power, i.e. $P_{peaki} >> P_{ave}(t)$, so that the counter-propagating effect can be neglected. Then, the relative power ratios of the pulse divided by the SDC will be given by the following equation.

$$P_{peak1} : P_{peak2} : \cdots : P_{peakN} = 1 : 2 : \cdots : 2^{N-1}. \tag{3.6}$$

On the other hand, the counter-propagating effect cannot be neglected in the cases of a A/D conversion with a high-sampling rate and/or a high-resolution.

3.4.2 Static Characteristics of the Encoder with Counter-propagating Effect

The second regime we consider is the case where the analog signal changes enough slowly as compared with τ, the transit time of the probe pulse in the NOLM. In this regime, the all control pulses in each time-slot in HNLF have approximately the same peak power at each instant of time, *t*. Then, P_{ave}, and hence the phase shift $\phi_{XPM\text{-}CCW}$, is approximately proportional to the peak power of the control pulses P_{peaki}. Here, let us define $R_P = P_{peak}/P_{ave}$, as the peak-to-average power ratio of the

input sampled analog pulse before entering the SDC. The average power of a control pulse train after the SDC, $P_{ave\text{-}SDC}$ is given by

$$P_{ave-SDC}(t) = \frac{P_{peak1}(t) + P_{peak2}(t) + \cdots + P_{peakN}(t)}{R_P}. \tag{3.7}$$

The relative power ratios of the divided control pulses by the SDC can be calculated using Eq. (3.4), (3.5) and (3.7).

$$P_{peak1} : P_{peak2} : P_{peak3} = 1 : \left(2 - \frac{7}{4 + R_P}\right) : \left(4 - \frac{21}{4 + R_P}\right) \tag{3.8}$$

For example, assuming that the pulse shape is of sech^2, the peak-to-average power ratio R_P can be written as

$$\begin{aligned} R_P &= \frac{P_{peak}(t)}{P_{ave}(t)} \\ &\approx \frac{1000 \times P_{peak}(t)}{0.5673 \times T_{FWHM} \times P_{peak}(t) \int_{-\infty}^{\infty} \mathrm{sech}^2(T) dT \times B} \\ &\approx \frac{881}{T_{FWHM} \times B} = Const., \end{aligned} \tag{3.9}$$

where T_{FWHM} [ps] is the full-width at half-maximum of the control pulse and B [GHz] is the repetition rate (sampling rate). If the control pulse width is 3 ps for 3-bit A/D conversion at 10 GS/s, the peak-to-average power ratio R_P is approximately 29.4. The relative power ratios of the control pulses are $P_{peak1} : P_{peak2} : P_{peak3}$ = 1 : 1.79 : 3.37.

3.4.3 Dynamic Characteristics of the Encoder with Counter Propagating Effect

While the second regime we have considered only very slowly varying analog signal input, the third regime that we consider here is the case where the input analog signal varies fast enough, but its average power defined in Eq. (3.2) can be approximated as a constant. This is usually the case for the optical signals used in high-speed data transmissions. For a constant average power of the control

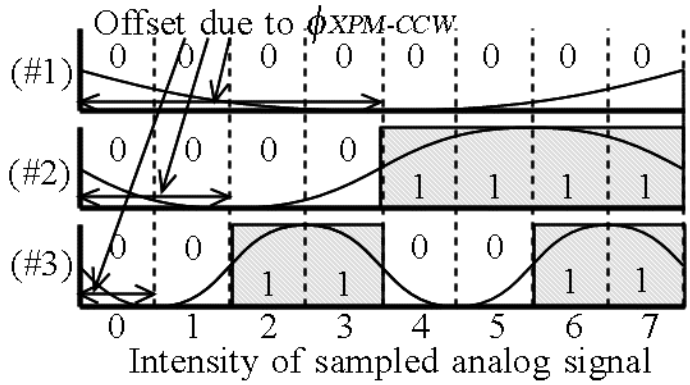

Fig. 3.5 Transfer functions of the encoder in the case of the counterclockwise probe pulses receive constant phase shift $\phi_{XPM\text{-}CCW} = \pi/2$.

pulses, the traveling counter-clockwise probe pulse trains always receive the same amount of phase shift $\phi_{XPM\text{-}CCW}$ irrespective of which time slot the probe pulse belongs to. Fig. 3.5 shows the transfer function with the constant phase shift $\phi_{XPM\text{-}CCW} = \pi/2$, and the relative power ratio of control pulse train are 1 : 2 : 4. The phase shift laterally translates the transfer functions. So the transfer function of the encoder cannot operate properly for quantizing and coding into Gray Code. The similar problems have also arisen in ultra-fast wavelength conversion and 3R regeneration using NOLM [29-31]. This problem can be solved by giving the same magnitude of the phase shift to the clockwise probe pulse train. If the HNLF in the encoder uses a non-polarization-maintaining HNLF, this effect can be compensated by the polarization controller of the encoder [29]. If the HNLF in the encoder uses polarization-maintaining HNLF, the solutions using an optical bias controller or optical phase-bias compensator (OPBC) have been studied [30, 31]. Therefore, when the analog signal does not contain low frequency components, these schemes can be applied to compensate the counter-propagating effect.

3.5 Numerical Simulation

In the previous section, we neglected the fiber loss, changes in pulse shape, parametric amplification and walk off due to the fiber dispersion to simplify the discussions. In order to take these effects into account and precisely design our proposed scheme in detail, we run numerical simulations. Figure 3.6 shows the simulation model of the encoder. In order to consider the walk-off and the parametric amplification in HNLF, we used split-step-Fourier-method. To simplify the

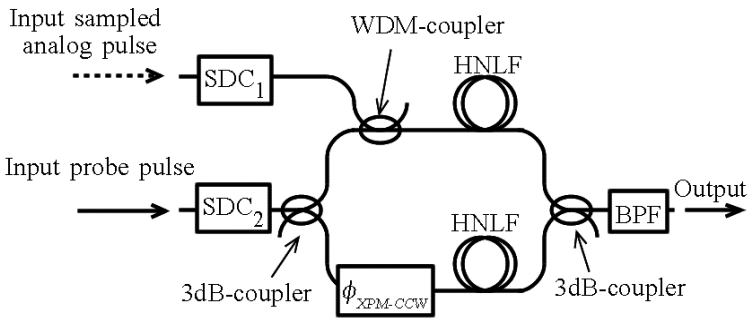

Fig. 3.6 Simulation model of the encoder.

Table 3.1 Parameters used in numerical simulation and experimental demonstration.

Input control pulse (Sampled Analog Pulse)	Pulse shape: $Sech^2$ Wavelength: 1560 nm Repetition rate: 10 GHz Pulse width: 4.78 ps
Input probe pulse	Pulse shape: $Sech^2$ Wavelength: 1570 nm Repetition rate: 10 GHz Pulse width: 2.45 ps Average power: 4 mW
Band pass filter	Filtering shape: Gaussian Center wavelength: 1570 nm -3dB band width: 3.2 nm
Parameters of HNLF in the encoder	
Fiber length L [m]	380
Nonlinearity γ [$W^{-1}km^{-1}$]	17.5
Zero dispersion wavelength λ_0 [nm]	1575
Dispersion slope λ_S [ps/km/nm^2]	0.0271
Fiber loss α [dB/km]	0.668
Excess loss of components	
3dB-coupler	0.05 dB
WDM-coupler at 1560nm	0.93 dB
WDM-coupler at 1570nm	0.82 dB

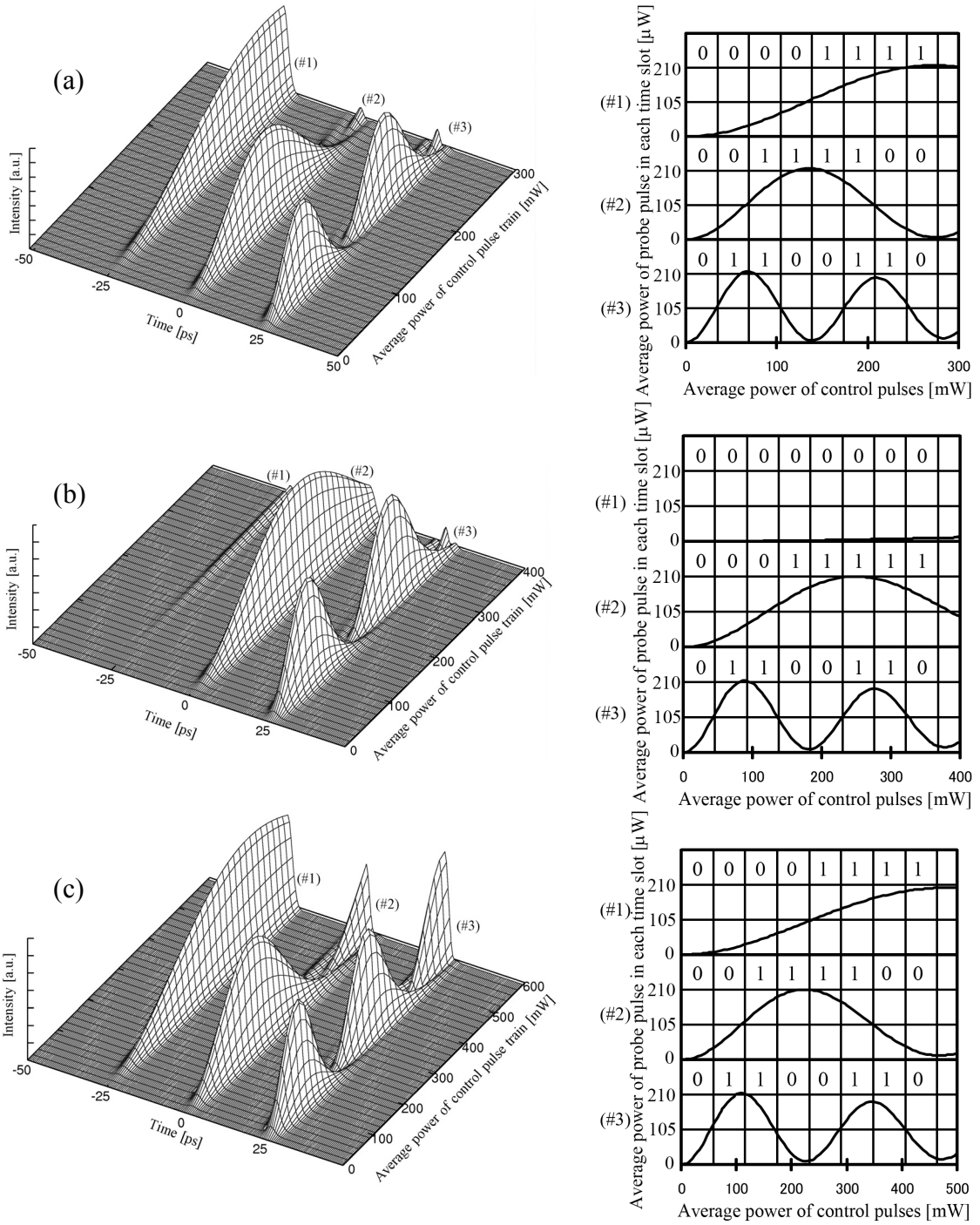

Fig. 3.7. Waveforms of each input power of control pulse train, and transfer functions in each time-slot of the proposed encoder for 3-bit quantizing and coding. The counter-propagating effect is neglected in (a), and included in (b) and (c). The relative power ratios of the control pulse train are (a) 1 : 2 : 4, (b) 1 : 2 : 4, and (c) 1 : 1.69 : 3.06, respectively.

simulation procedure, we split the counter-clockwise and clockwise path into two different paths. The control pulses and the probe pulses are input to the upper side path through WDM coupler and 3-dB coupler, respectively, for simulating the clockwise path. In the lower side path, only the probe pulses are input through the 3-dB coupler, for simulating the counter-clockwise path. The timing of input probe pulses is adjusted to maximize XPM under the effect of walk-off. It is assumed that the control and probe pulses maintain the same polarization state. We should note that the effects of bidirectional propagation cannot be simulated by this simplified model. However, in order to consider the counter-propagating effect, the phase shift $\phi_{XPM\text{-}CCW}$ by the average power of the control pulses is added to the probe pulse in counter-clockwise path. The connection loss of fibers were neglected. The SDCs divide one pulse to three pulses by a 25-ps time delay. Table 3.1 shows the parameters used in the numerical simulations. All of the parameters are the same as those of the experimental demonstrations described in the subsequent section.

Fig. 3.7(a) shows the waveforms of each input power of control pulse train, and transfer functions of each time-slot for the case that the counter-propagating effect is neglected ($\phi_{XPM\text{-}CCW} = 0$) and the relative power ratios of the control pulse train are P_{peak1}: P_{peak2}: P_{peak3} = 1 : 2 : 4. Fig. 3.7(b) shows the waveforms of each input power of control pulse train, and the transfer functions of each time-slot including the counter-propagating phase shift $\phi_{XPM\text{-}CCW} = 2\gamma L_{eff} P_{ave}$ and the relative power ratios of the control pulses are P_{peak1}: P_{peak2}: P_{peak3} = 1 : 2 : 4, where L_{eff} is the effective length defined as L_{eff} = (1-exp(-αL))/α. Fig. 3.7(c) shows the waveforms of each input power of control pulse train, and the transfer functions of the probe pulses at each power of the control pulses for the case that the counter-propagating effect is included ($\phi_{XPM\text{-}CCW} = 2\gamma L_{eff} P_{ave}$) and the ratios of the control pulse train are P_{peak1}: P_{peak2}: P_{peak3} = 1 : 1.69 : 3.06 in accordance with Eq. (3.8).

When the counter propagating effect is neglected, the encoder exhibits a (#1) half-, (#2) single- and (#3) two-period transfer function for each time-slot of an input analog pulse as shown Fig. 3.7(a). When the counter-propagating effect is considered, and the relative power ratios are P_{peak1}: P_{peak2}: P_{peak3} = 1 : 2 : 4, the transfer functions of each time-slot is distorted resulting in errors in quantization and coding as shown Fig. 3.7(b). On the other hand, by properly setting the power ratios of the control pulses to be 1 : 1.69 : 3.06, respectively, the transfer functions of each time-slot fitted for A/D conversion as shown Fig. 3.7(c). The output power does not become 0 mW at the points where the phase difference $\Delta\phi$ became 2π and 4π. Due to the walk-off between the control pulse and the probe pulse, and because the shape of the control pulse is not rectangular, the control pulse cannot cause the XPM uniformly over the entire probe pulse.

3.6 Experimental Demonstration

Figure 3.8 shows the experimental setup for demonstrating our proposed 3-bit all-optical quantizing and coding at a sampling rate of 10 GS/s using split-and-delay technique, and table 3.1 shows the parameters used in the above numerical simulations that are completely the same as those used in this experiment. We used a 10 GHz mode-locked fiber ring laser (FRL) operating at a wavelength of 1560 nm with a pulse width of 2.48 ps for the pulse sources of the control pulses and the probe pulses. We generated the probe pulses by means of the wavelength conversion through four-wave mixing (FWM) in $HNLF_1$ with the pulse source and a tunable laser source (TLS) whose wavelength is set at 1550 nm. The probe pulses, which are generated at a wavelength of 1570 nm with a pulse width of 2.45 ps, are synchronized with the control pulse. Split-and-delay couplers (SDCs) were used to divide one pulse into three pulses with 25-ps spacing. The SDC for control pulse (SDC_1) was set to provide the different phase shift $\Delta\phi_{XPMi}$ (i =1, 2, 3) with the ratio of 1 : 2 : 4, respectively. The SDC for probe pulse (SDC_2) was used to divide pulses with a same intensity synchronized with the split control pulse train. The BPF_1 with a 3-dB bandwidth of 0.532 nm was used to expand the pulse width of the control pulse train up to 4.78 ps. The variable optical attenuator (VOA) was used to emulate the change level of the optical analog signal input. In this experiment, we measured the only static characteristics of the A/D converter, because the VOA cannot make a fast varying analog signal. The variable delay line (VDL) was set so as to overlap the probe pulse train with the control pulses. The two PCs at each input matched the polarization states of the control pulses and the probe pulses, for XPM efficiently inducing. The PC in the loop was used to adjust the bias setting so that all probe pulses were output to the reflection port, when the control pulses are absent. The BPF_3 placed at the NOLM output removed the control pulses and only transmits the probe pulses.

At first, in order to adjust the encoder, We set the experimental setup without dividing pulses at the SDCs. We set the relative power ratios of each SDC in 1 : 0 : 0. The PC in the loop was adjusted to reflect the probe pulses when the control pulses are not inputted, and the VDL was adjusted to make the probe pulses overlap with the control pulses, and the two PCs of each input port was adjusted to make the polarization states of the control pulses match with that of the probe pulses for maximizing the XPM. Then, We introduced the SDCs. The SDC_2 was adjusted to divide the probe pulses with the same intensity. The relative power ratios of SDC_1 were adjusted to provide the different phase shifts $\Delta\phi_{XPMi}$ (i =1, 2, 3) with ratios of 1 : 2 : 4, respectively. Here, the average power of the control pulses and the relative power ratios were adjusted alternately so that each intensity of the transmitted

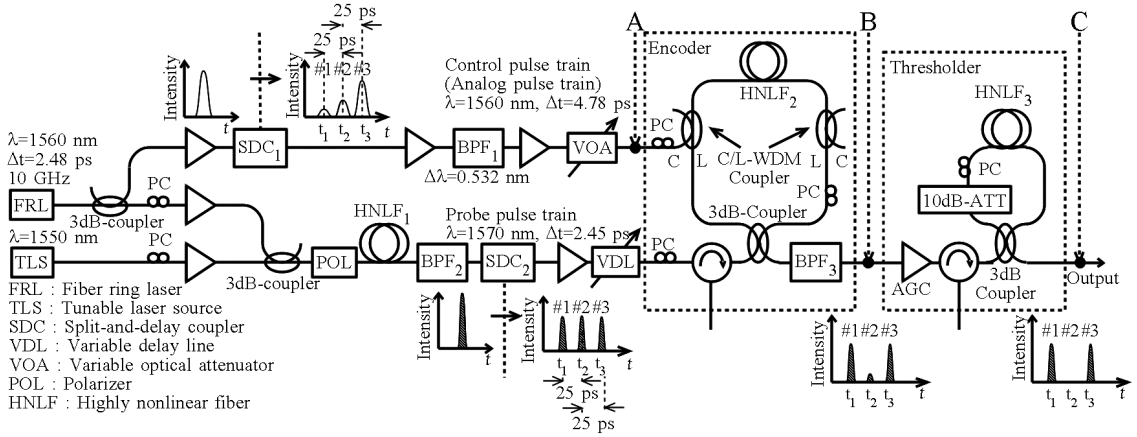

Fig. 3.8 Experimental setup for the proposed 3-bit quantizing and coding at a sampling rate of 10 GS/s using split-and-delay technique.

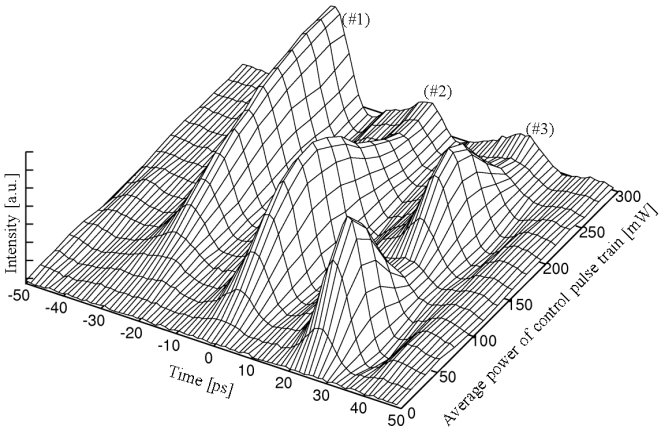

(a) Sampling oscilloscope traces without thresholder.

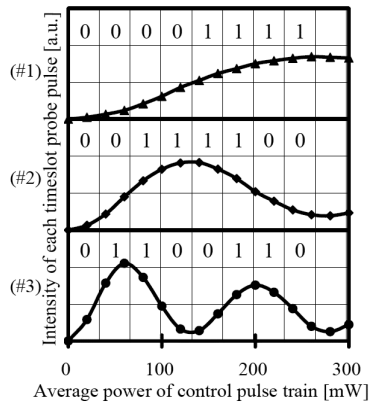

(b) Transfer functions in each time-slot without thresholder.

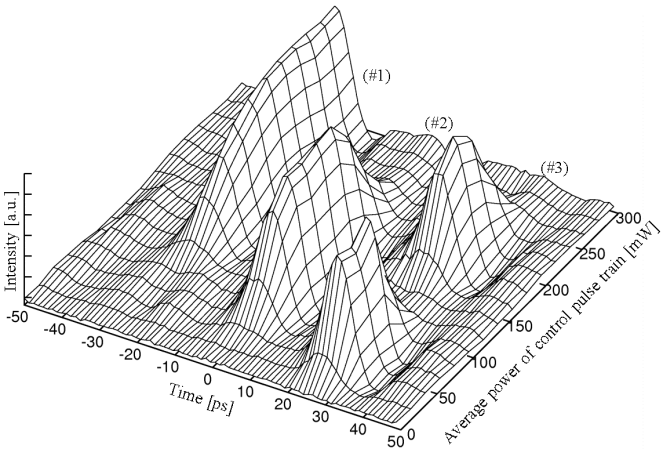

(c) Sampling oscilloscope traces with thresholder.

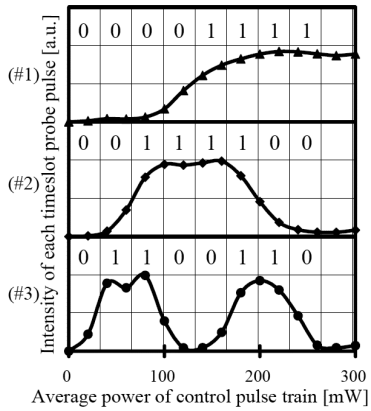

(d) Transfer functions in each time-slot with thresholder.

Fig. 3.9 Experimental results.

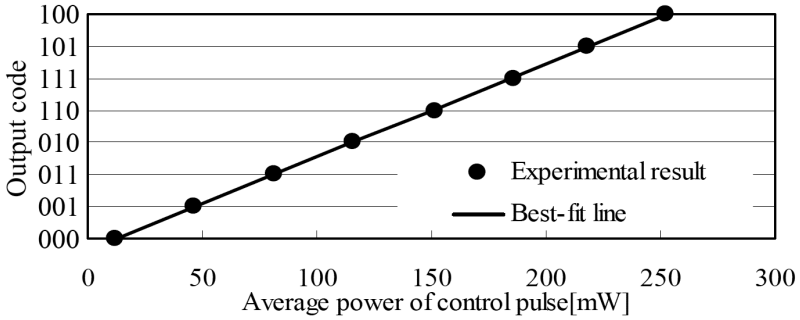

Fig. 3.10 Transfer function of the encoder.

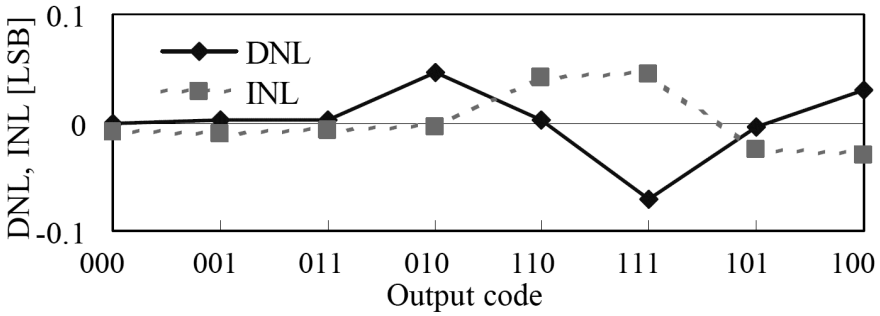

Fig.3.11 Measured DNL and INL of the encoder.

probe pulse was became half for $\Delta\phi_{XPM1} = \pi/2$, local maximum for $\Delta\phi_{XPM2} = \pi$, and local minimum for $\Delta\phi_{XPM3} = 2\pi$ in each time-slot #1, #2 and #3 respectively. The resulting relative power ratios of the divided control pulses P_{peak1}: P_{peak2}: P_{peak3} were measured to be 1 : 1:84 : 3.79, respectively. This is not equal to the theoretical result using Eq. (3.8). This discrepancy is probably due to the mismatching of the polarization states between the control pulse train and counter-propagating probe pulse train in $HNLF_2$. The mismatching reduces the counter propagating effect due to reducing the amount of the XPM suffered by the counter-propagating probe pulses.

The measured sampling oscilloscope traces and transfer functions of the encoder without the thresholder (point B in Fig. 3.8) are shown in Fig. 3.9(a) and Fig. 3.9(b). The average power of the control pulses was measured at the output of VOA (point A in Fig. 3.8). The transfer functions were measured by reading the peak power of the sampling oscilloscope traces in each time-slot.

The (#1)half-, (#2)single- and (#3)two-periods transfer functions were observed. Compared with the simulation result, the input power required in the experiment was 1.4 dB larger. The difference may have come from the splice loss of the fiber, and the misalignment of polarization states of the control pulses and the probe pulses. A self-switching NOLM was used for the thresholder. The length and nonlinear coefficient of $HNLF_3$ are 830 m, and 19 $W^{-1}km^{-1}$, respectively. The EDFA in

the thresholder operated in a constant gain mode avoiding its transient effects. The measured sampling oscilloscope traces and transfer functions of the encoder with the thresholder (point C in Fig. 3.8) are shown in Fig. 3.9(c) and Fig. 3.9(d). We note that the width of the output probe pulses from the encoder measured with an autocorrelator were approximately 2.0 ps. The pulse widths in Fig. 3.9 were wider than 2.0 ps, due to the limited bandwidth of the photo detector and the sampling oscilloscope. The transfer function, differential nonlinearity (DNL) and integral nonlinear nonlinearity (INL) of the encoder are shown in Fig. 3.10 and fig. 3.11. Fig. 3.10 shows the offset error of 12.4 mW. Fig 3.11 shows a peak DNL of 0.070 LSB and a maximum INL of 0.045 LSB.

3.7 Conclusion

In this chapter, we have proposed a split-and-delay technique for simplification of the multi-bit A/D conversion and discussed detailed design issues of the encoder accounting for the counter-propagating effects in the case of slow and fast varying analog signals. With this technique, sampling rate and resolution of A/D converter changed easily, and the convenience of the all-optical A/D converter increases. We have succeeded in the experimental demonstration of our proposed scheme to realize the quantizing and coding of 3-bit A/D conversion at 10 GS/s. However, in this experimental demonstration, we measured the only static characteristics of the A/D converter. To realize a high-speed signal A/D conversion, a demonstration using a fast varying analog signal has yet to be studied in the future.

Chapter 4

Ultrafast Versatile All-Optical Logic Gate using Nonlinear Optical Loop Mirrors

4.1 Introduction

In this chapter, we propose and experimentally demonstrate a versatile all-optical logic gate capable of all sixteen two-input logic operations without changing the configuration. This scheme can perform respective logic operations only by adjusting polarization controllers and variable optical attenuators without changing the configuration. This scheme provides flexibility with ultrafast operation in optical communications. In section 4.2, we review the principle of the versatile all-optical logic gate. In section 4.3, the experimental demonstrations are all-optical logic operations of AND, NAND, OR, NOR, XOR, and XNOR at 40 Gbit/s. In section 4.4, we consider the limitation of the processing speed due to dispersion and undesirable nonlinear effects in HNLF, and show the feasibility of the processing speed up to 350 Gbit/s by numerical simulations.

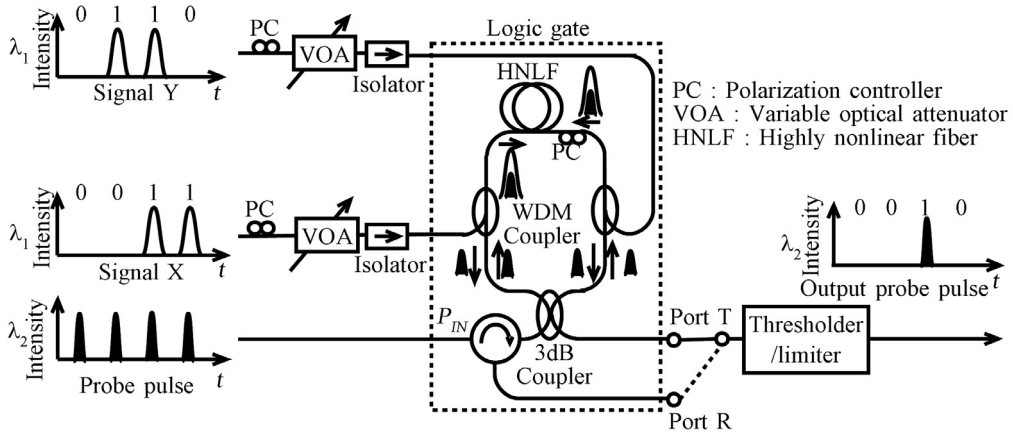

Fig. 4.1 Configuration of versatile all-optical logic gate.

4.2 Principle Operation of Versatile All-Optical Logic Gate

The configuration of the proposed optical logic gate is shown in Fig. 4.1. The logic gate operation is realized through a bidirectional-input nonlinear optical loop mirror based switch and a thresholder/limiter. The thresholder/limiter follows this switch in order to eliminate the incomplete suppression of nulls and non-uniform height of ones for the sake of the sinusoidal nature of nonlinear-optical-loop-mirror (NOLM) switching. The input RZ signals X and Y at a wavelength of λ_1 are launched into the loop via the WDM couplers as clockwise and counter-clockwise travelling control pulses, respectively. The output is obtained from either port T or R depending on the type of logic operation to be realized. Variable attenuators (VOAs) are used to adjust the input powers. The phase shifts ϕ_{CW} and ϕ_{CCW}, which are induced by the input signals X and Y are given by

$$\phi_{CW} = 2\gamma P_X L, \tag{4.1}$$

$$\phi_{CCW} = 2\gamma P_Y L, \tag{4.2}$$

respectively, where γ and L are the nonlinear coefficient and length of the highly non-linear fiber (HNLF), respectively. P_X and P_Y are the peak power of the signal X and Y, respectively. The electric fields E_{CW}, E_{CCW} of clockwise and counter-clockwise traveling probe pulse after passing through the HNLF are given by

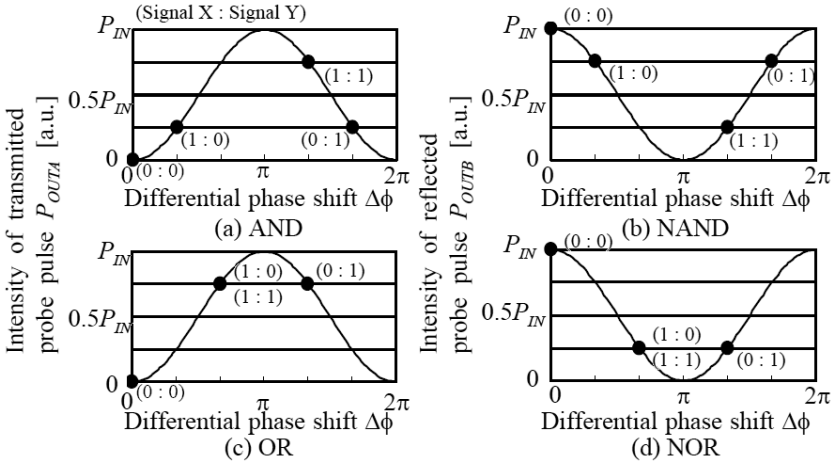

Fig. 4.2 Variable logic operation.

Table 4.1 Phase shift amount for all two-input logic operation.

Logic operation	ϕ_{CW} [rad]	ϕ_{CCW} [rad]	Output port	Output level (Output power) at input signal X:Y			
				1:1	1:0	0:1	0:0
0	0	0	Port T	0 (0)	0 (0)	0 (0)	0 (0)
$\overline{X+Y}$ (NOR)	2π/3	4π/3	Port R	0 ($0.25P_{IN}$)	0 ($0.25P_{IN}$)	0 ($0.25P_{IN}$)	1(P_{IN})
$\overline{X} \bullet Y$	π/3	2π/3	Port T	0 ($0.25P_{IN}$)	0 ($0.25P_{IN}$)	1 ($0.75P_{IN}$)	0 (0)
$\overline{X}$	π	0	Port R	0 (0)	0 (0)	1 (P_{IN})	1 (P_{IN})
$X \bullet \overline{Y}$	2π/3	π/3	Port T	0 ($0.25P_{IN}$)	1 ($0.75P_{IN}$)	0 ($0.25P_{IN}$)	0 (0)
$\overline{Y}$	0	π	Port R	0 (0)	1 (P_{IN})	0 (0)	1 (P_{IN})
$X \oplus Y$ (XOR)	π	π	Port T	0 (0)	1 (P_{IN})	1 (P_{IN})	0 (0)
$\overline{X \bullet Y}$ (NAND)	π/3	5π/3	Port R	0 ($0.25P_{IN}$)	1 ($0.75P_{IN}$)	1 ($0.75P_{IN}$)	1 (P_{IN})
$X \bullet Y$ (AND)	π/3	5π/3	Port T	1 ($0.75P_{IN}$)	0 ($0.25P_{IN}$)	0 ($0.25P_{IN}$)	0 (0)
$\overline{X \oplus Y}$ (XNOR)	π	π	Port R	1 (P_{IN})	0 (0)	0 (0)	1 (P_{IN})
Y	0	π	Port T	1 (P_{IN})	0 (0)	1 (P_{IN})	0 (0)
$X + \overline{Y}$	2π/3	π/3	Port R	1 ($0.75P_{IN}$)	0 ($0.25P_{IN}$)	1 ($0.75P_{IN}$)	1 (P_{IN})
X	π	0	Port T	1 (P_{IN})	1 (P_{IN})	0 (0)	0 (0)
$\overline{X} + Y$	π/3	2π/3	Port R	1 ($0.75P_{IN}$)	1 ($0.75P_{IN}$)	0 ($0.25P_{IN}$)	1 (P_{IN})
$X + Y$ (OR)	2π/3	4π/3	Port T	1 ($0.75P_{IN}$)	1 ($0.75P_{IN}$)	1 ($0.75P_{IN}$)	0 (0)
1	0	0	Port R	1 (P_{IN})	1 (P_{IN})	1 (P_{IN})	1 (P_{IN})

$$E_{CW} = \frac{1}{\sqrt{2}} E_0 \exp(i\phi_{CW}), \tag{4.3}$$

$$E_{CCW} = \frac{i}{\sqrt{2}} E_0 \exp(i\phi_{CCW}), \tag{4.4}$$

respectively, where E_0 is input electric field of the probe pulse. The electric field of the output probe pulse E_{OUT} is given by

$$\begin{aligned} E_{OUTT} &= \frac{1}{\sqrt{2}} \bullet \frac{1}{\sqrt{2}} E_0 \exp(i\phi_{CW}) \\ &+ \frac{i}{\sqrt{2}} \bullet \frac{i}{\sqrt{2}} E_0 \exp(i\phi_{CCW}) \\ &= \frac{E_0}{2} \left[\exp(i\phi_{CW}) - \exp(i\phi_{CCW}) \right] \end{aligned} \tag{4.5}$$

$$\begin{aligned} E_{OUTR} &= \frac{i}{\sqrt{2}} \bullet \frac{1}{\sqrt{2}} E_0 \exp(i\phi_{CW}) \\ &+ \frac{1}{\sqrt{2}} \bullet \frac{i}{\sqrt{2}} E_0 \exp(i\phi_{CCW}) \\ &= \frac{iE_0}{2} \left[\exp(i\phi_{CW}) + \exp(i\phi_{CCW}) \right] \end{aligned} \tag{4.6}$$

The peak powers of the output probe pulses can be written as

$$P_{OUTT} = \frac{1}{2} P_{IN} \left\{ 1 - \cos\left(\Delta\phi\right) \right\}, \tag{4.7}$$

$$P_{OUTR} = \frac{1}{2} P_{IN} \left\{ 1 + \cos\left(\Delta\phi\right) \right\}, \tag{4.8}$$

where P_{IN} is the peak power of the input probe pulse, P_{OUTT} and P_{OUTR} are the peak powers of the output probe pulses at the transmission and reflection ports, respectively, $\Delta\phi$ is the phase difference between the clockwise as

$$\Delta\phi = |\phi_{CW} - \phi_{CCW}|. \quad (4.9)$$

The transfer function of the NOLM switch depends on the differential phase shift. For example, when signal X is "1" level, the clockwise travelling probe pulse induces a phase shift due to the cross phase modulation (XPM) in HNLF. For signal Y at "1" level, the counter-clockwise travelling probe pulse also induces a phase shift. The phase shifts become null for the cases of "0" signal inputs. A variety of logic operations can be realized by properly setting the values of the phase shifts ϕ_{CW} and ϕ_{CCW}, that are in proportion with the peak power of the input signals. The phase shifts due to the input "1" signal for all two-input logic functions are summarized in Table 4.1. For example, Fig. 4.2 shows the transfer functions and operating points of NOLM for logic operations of AND, NAND, OR, and NOR. The output of OR operation is obtained from the transmission port P_{OUTT} by setting the phase shifts ϕ_{CW} and ϕ_{CCW} to be $2\pi/3$ rad and $4\pi/3$ rad, respectively. Note that the input peak powers are represented in two ways, the logical values 0 or 1 and the actual values in the bracket. When, input signals (X:Y) are (0:0), (0:1), (1:0), and (1:1), the peak powers of transmitted probe pulse P_{OUTT} becomes 0, $0.75P_{IN}$, $0.75P_{IN}$, and $0.75P_{IN}$, respectively, as shown in Fig. 4.2(c).

4.3 Experimental demonstration

Figure 4.3 shows the experimental setup for the all-optical logic gate operating at 40 Gb/s. we used a 10-GHz mode-locked fiber ring laser (FRL) operating at a wavelength of 1560 nm and a time width of 3.1 ps for a pulse source of the control pulses and the probe pulses. The first optical time division multiplexer (OMUX1) with a time interval of 25 ps generated control pulse sequences of {0011} and {0110} at 40 Gb/s. we generated probe pulses from wavelength conversion of the control pulse sequences of {0011} in $HNLF_1$ through the four-wave mixing with the continuous wave signal light of 1550 nm tunable laser source (TLS). And the following OMUX2 with 50-ps time interval generated a pulse sequence of {1111} at 40 Gb/s. The probe pulses have a carrier wavelength of 1570 nm, a pulse width of 2.6 ps, and are synchronized with the signal pulse bit sequences. The BPF1 with 3-dB bandwidth of 0.34 nm was used to expand the width of each control pulse up to 9.7 ps. The variable optical delay lines (VDL) were adjusted for fixed signal pattern of (X:Y) = (0:0), (0:1), (1:1), and (1:0) at each time slot. The peak powers of input signals X and Y are adjusted to the phase shifts ϕ_{CW} and ϕ_{CCW} of each logic operation by the VOAs, as

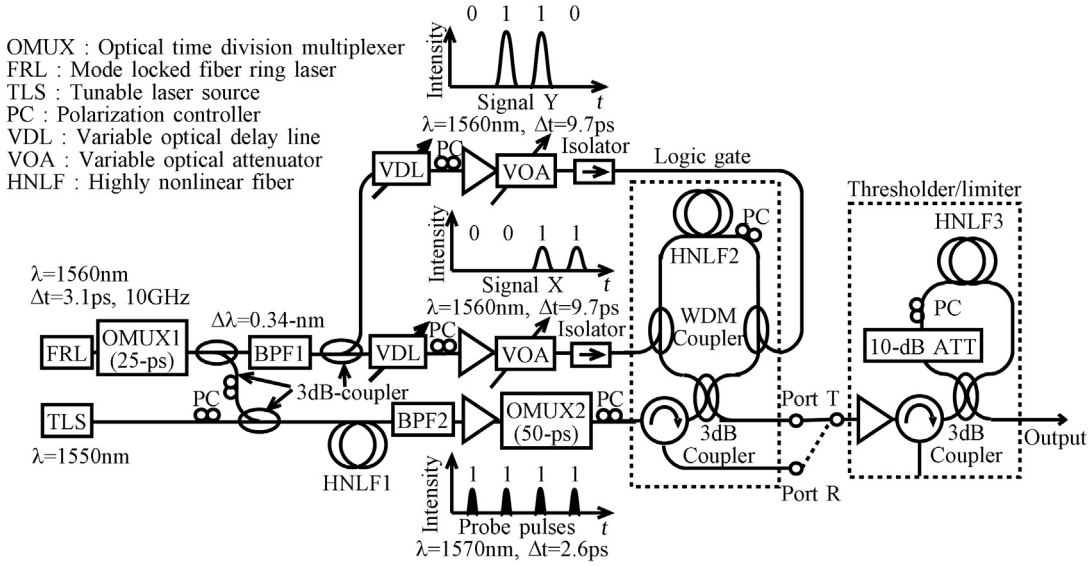

Fig. 4.3 Experimental setup.

shown in table 4.1. The fiber length L and the nonlinear coefficient γ of $HNLF_2$ of the logic gate were 380 m and 17.5 $W^{-1}km^{-1}$, respectively. The second-stage NOLM was used as a thresholder/limiter. The gain of EDFA and PC in the thresholder/limiter were adjusted to suppress "0" level signals, and stabilizing fluctuations of "1" level signals. The fiber length L and the nonlinear coefficient γ of $HNLF_3$ were 830 m and 19 $W^{-1}km^{-1}$, respectively.

Figures 4.4 and 4.5 show the waveforms of output probe pulses before and after the thresholder/limiter, respectively. Table 4.2 shows the extinction ratios of output probe pulses before and after the thresholder/limiter, respectively. These waveforms were measured with a photo detector and a sampling oscilloscope. The logic operations AND, NAND, OR, NOR, XOR, and XNOR were successfully obtained, as the thresholder/limiter suppressed "0" level signals and tailored "1" level signals. The extinction ratios were improved to over 8.6 dB by the tresholder/limiter. We note that the width of the output probe pulse from the logic gate and the thresholder/limiter measured with an autocorrelater was 2.8 ps. The pulse widths in figures 4.4 and 4.5 were wider than 2.8 ps, due to the limited bandwidth of the photo detector and the sampling oscilloscope.

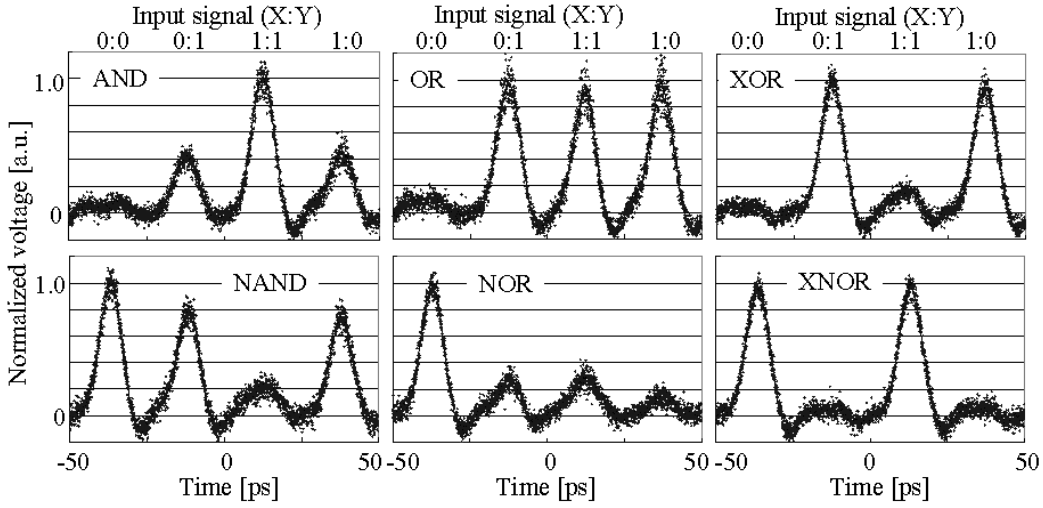

Fig. 4.4 Sampling oscilloscope traces of output probe pulse in each logic operation before the thresholder/limiter.

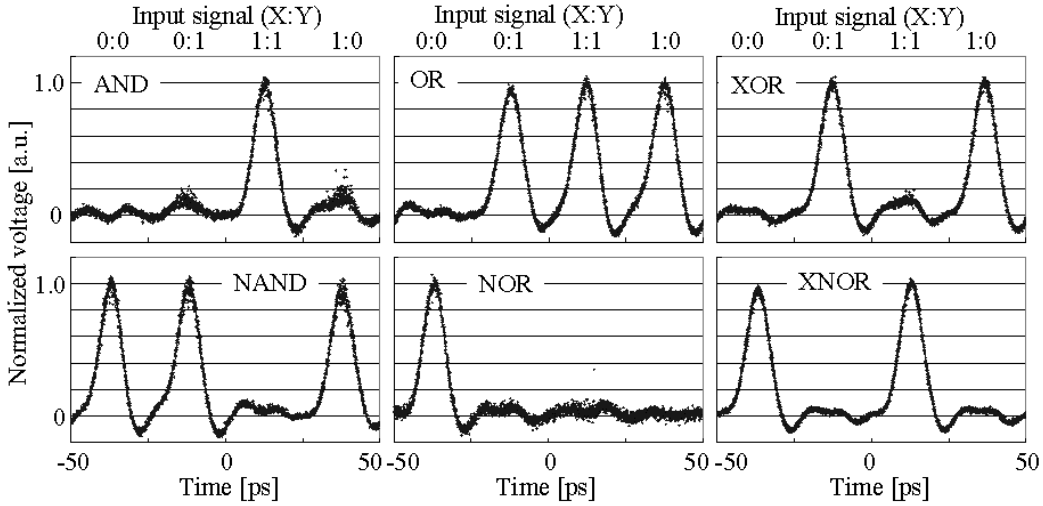

Fig. 4.5 Sampling oscilloscope traces of output probe pulse in each logic operation after the thresholder/limiter.

Table 4.2 Extinction ratios in each logic operation before and after the thresholder/limitter.

Logic operation	Before	After
AND	3.5 dB	8.6 dB
OR	9.2 dB	14.9 dB
XOR	7.5 dB	9.4 dB

Logic operation	Before	After
NAND	5.4 dB	13.1 dB
NOR	5.4 dB	11.7 dB
XNOR	12.3 dB	13.8 dB

Table 4.3 Simulation parameters.

HNLFs parameters		
	$HNLF_1$	$HNLF_2$
Fiber loss [dB/km]	0.5	0.5
Zero dispersion wavelength λ_0 [nm]	1565	1576.5
Dispersion slope [ps/km-nm^2]	0.02	0.02
Nonlinearity [1/W-km]	12.0	12.0
Fiber length [km]	0.5	0.5
BPF parameters		
Bandwidth [nm]	5	
Filter shape	Gaussian	
Probe pulse parameters		
Pulse width [ps]	0.5	
Pulse shape	Sech^2	
Peak power [W]	0.01	

Table 4.4 wavelength spacing and peak powers.

Initial pulse width [ps]	Wavelength spacing $\Delta\lambda$ [nm]	Peak power [W]	
		Signal X	Signal Y
0.5	36	0.20	1.18
0.6	30	0.16	0.96
0.7	26	0.14	0.82
0.8	23	0.13	0.75
0.9	21	0.12	0.69
1.0	20	0.12	0.68
1.1	18	0.11	0.65

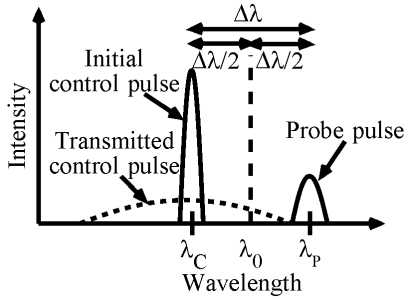

Fig. 4.6 Wavelength allocation.

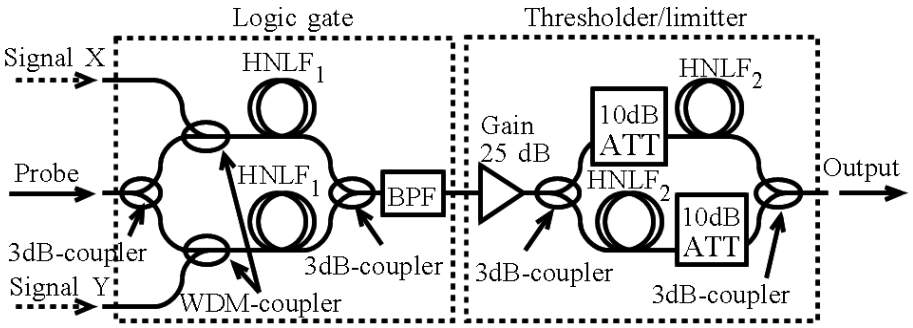

Fig. 4.7 Simulation model.

4.4 Discussion

In this section, we discuss the limitation of processing speed due to group velocity dispersion (GVD) and self-phase-modulation (SPM) in HNLF. In order to suppress an inter-symbol interference (ISI), the time slot has to be wider than the pulse width of the control pulse through the HNLF. The GVD has to be carefully designed for ultrafast operation, because the wavelengths of

the control and probe pulses are allocated in the normal and the anomalous dispersion regions in order to suppress the walk-off effect, as shown in Fig. 4.6. The temporal shapes of the control pulses are also changed by the interaction of GVD and SPM. Therefore, we need to optimize the peak power and the pulse width of control pulses considering the dispersion profile and the nonlinearity of HNLF, while at the same time the spectral broadening of the control pulse caused by SPM has to be taken into account. If the wavelength spacing $\Delta\lambda$ between the control and probe pulse is too narrow, the broadened spectrum of the control pulse overlaps with that of the probe pulse. If the wavelength spacing is too wide, the control pulse is greatly broadened due to the large GVD.

We investigate the minimum time slot determined by the interaction of GVD and SPM for the parameters of a currently available HNLF by numerical simulation. Table 4.3 shows the parameters of HNLFs, a BPF and the probe pulse. Here, we simulated the case of AND operation, because AND and NAND operations are the most difficult ones due to the largest phase shift of $5\pi/3$. Figure 4.7 shows the simulation model of the logic gate and the thresholder/limitter. In order to consider the GVD and nonlinearity in a HNLF, we used split-step-Fourier-method. To simplify the simulation procedure, we split the counter-clockwise and clockwise path into two different paths. Table 4.4 shows the minimum wavelength spacing to avoid overlap of the broadened spectrum of the control pulse, and the peak powers of signals X and Y at each initial pulse width. The peak powers of signal X and Y differ from the initial pulse width, because decreasing of the peak powers by dispersion effects passing through the HNLF depends on the initial pulse width. Figure 4.8 shows the -3 dB and -13 dB pulse width of signal Y after passing through the HNLF against the initial pulse width. The shape of a control pulse becomes nearly rectangular due to an interaction of the GVD and nonlinear effect. Therefore, the width of time slot can set shorter than twice -3dB width without the effect of ISI. Here, we define the -13 dB pulse width of transmitted signal Y as the minimum width of a time slot, because the powers of output probe pulses with the effect of the bit pattern are stable enough. The -13 dB width has the minimum value of 2.85 ps when the initial pulse width is 0.8 ps. The processing speed can be up to 350 Gbit/s with currently available HNLF. Figure 4.9 shows the input and output waveforms of the AND operation for the input pulse with a temporal width of 0.8 ps, and for a processing speed of 350 Gbit/s. Theses results show that the ISI effect in the logic gate is very small. The extinction ratio of output probe pulses was improved to 13.7 dB from 5.0 dB by the thresholder/limitter.

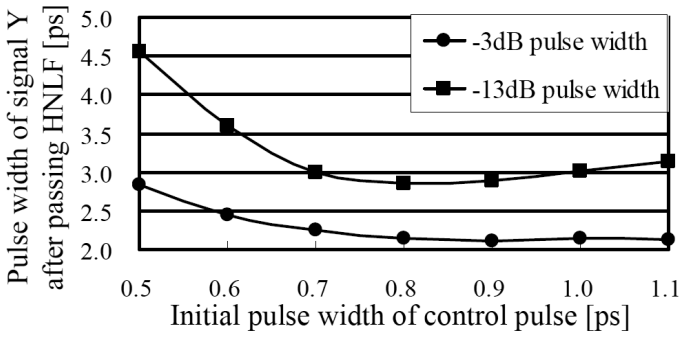

Fig. 4.8 Pulse width of signal Y after passing through the HNLF.

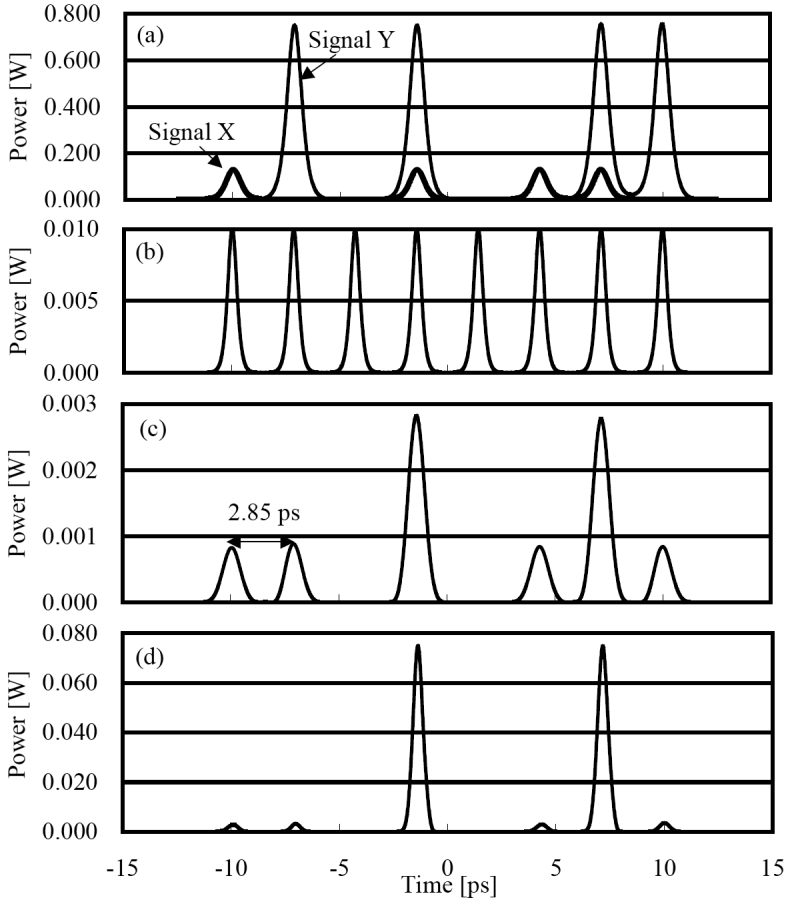

Fig. 4.9 Simulation results: Waveforms of (a) signal X and Y, (b) probe pulse, and (c) output signal before the thresholder/limiter, (d) output signal after the thresholder/limiter.

4.5 Conclusion

In this chapter, we have proposed a versatile all-optical logic gate based on multi-periodic transfer function of a NOLM. We have shown that the proposed scheme can perform all sixteen two-input logic operations only by adjusting PCs and VOAs without changing the configuration. We have also experimentally demonstrated all-optical AND, NAND, OR, NOR, XOR, and XNOR operations at the processing speed of 40 Gbit/s. It has been found that the control and probe pulses with short temporal widths and a carefully designed wavelength allocation are required for realizing an ultrafast logic gate. We show the feasibility of the processing speed and the extinction ratio up to 350 Gbit/s and 13.7 dB by numerical simulation, respectively. The processing speed can be future improved by decreasing the dispersion slope and the fiber length of the HNLF. This logic gate will be able to process ultrafast optical signals without demultiplexing in optical-time-division-multiplex (OTDM) communication systems.

Chapter 5

Conclusions

This thesis has been devoted to investigate ultrafast all-optical A/D conversions and logic operations, which aim to be free from the speed limitation of electrical devices. In the future optical communication systems, to increase the bit rate of optical transmission systems, ultrafast A/D conversion is required for dispersion compensation techniques and advanced modulation format using digital signal processing, and to provide flexible photonic network, ultrafast all-optical logic gate is required for several signal processing in photonic routers. The main results obtained in this dissertation are summarized as follows:

In Chapter 2, an optical quantizing and coding scheme using multi-period transfer functions of NOLM have been introduced. In previous work, the number of bit resolution of A/D conversion was only 3-bit, which was not sufficient for optical communication systems. We investigated numerical design considerations of NOLMs, which is a key to the optical quantizing and coding. We consequently demonstrated a record, nearly 4-period transfer function for a control pulse width of approximately 2 ps capable of 4-bit A/D conversion at the sampling rate of 100 GS/s. Finally we demonstrated nearly 8-period transfer function of NOLMs. In the future, the 5-bit A/D conversion will be possible.

In Chapter 3, a split-and-delay technique for simplification of the multi-bit A/D conversion have been proposed, and detailed design issues of the encoder accounting for the counter-propagating effects in the case of slow and fast varying analog signals have been discussed. With this technique, sampling rate and resolution of A/D converter can be changed easily, and the convenience of the all-optical A/D converter increases. We have succeeded in an experimental demonstration of our proposed scheme to realize the quantizing and coding of 3-bit A/D conversion at the sampling rate of 10 GS/s.

In Chapter 4, a versatile all-optical logic gate based on multi-periodic transfer function of a NOLM has been proposed. We have shown that the proposed scheme can perform all sixteen two-input logic operations only by adjusting PCs and VOAs without changing the configuration. The flexibility and ultrafast operation are expected to support the digital signal processing in the photonic router of future optical communication systems. We have also experimentally demonstrated

all-optical AND, NAND, OR, NOR, XOR, and XNOR operations at a processing speed of 40 Gbit/s. It has been found that the control and probe pulses with short temporal widths and a carefully designed wavelength allocation are required for realizing an ultrafast logic gate. We show the feasibility of the processing speed up to 350 Gbit/s by numerical simulations.

From all the obtained result, it is conclude that, the proposed all-optical A/D conversion and logic operation have the feasibilities of ultrafast and flexible operation. Each proposed techniques are expected to support several digital signal processing for advanced future optical communication networks.

Bibliography

[1] H. Nosaka, M. Nakamura, M. Ida, K. Kurishima, T. Shibata, M. Tokumitsu, and M. Muraguchi, "A 24-Gsps 3-bit Nyquist ADC using InP HBTs for electronic dispersion compensation," in proc. IEEE/MTTS International Microwave Symposium TU5A-1, pp. 101-104, June 2004,.

[2] M. Okiura, S. Iguchi, S. K. Okumura, M. Momose, K. Matsumoto, and N. Kawaguchi, "Development of 4-Gsps 2-bit ADC with GaAs ICs for radio astronomy," in proc. IEEE/MTTS International Microwave Symposium, IF-TU-29, pp. 485-488, June 2002.

[3] K. Azadet, E. F. Haratsch, H. Kim, F. Saibi, J. H. Saunders, M. Shaffer, L. Song, and M. Yu, "Equalization and FEC technique for optical transceivers," IEEE J. Solid-State Circuits, vol. 37, pp. 317-327, Mar. 2002.

[4] H. F. Haunstein, S. Wolfgang, A. Dittrich, K. Sticht, R. Urbansky, **"**Principles for electronic equalization of polarization-mode dispersion," IEEE/OSA J. Lightwave Technology, vol. 22, no. 4, pp. 1169-1182, Apr., 2004.

[5] T. Foggi, E. Forestieri, G. Colavolpe, G. Prati**, "**Maximum-likelihood sequence detection with closed-form metrics in OOK optical systems impaired by GVD and PMD," IEEE J. Lightwave Technology, vol. 24, no. 8, pp. 3073-3087, Aug. 2006.

[6] B. L. Shoop, "photonic Analog-to-Digital Conversion, Berlin: Splinger-Verlag, 2001.

[7] T. Yamamoto, E. Yoshida, and M. Nakazawa, "Ultrafast nonlinear optical loop mirror for demultiplexing 640 Gbit/s TDM signals," IEE Electronics Letters, vol. 34, no. 10, pp. 1013–1014, May 1998.

[8] T. Fjelde, A. Kloch, D. Wolfson, B. Dagens, A. Couelin, I. Guillemot, F.Gaborit, F. Poingt, and M. Renaud, "Novel Scheme for Simple Label-Swapping Employing XOR Logic in Integrated

Interferometric Wavelength Converter," IEEE Photonics Technology Letters, vol. 13, no. 7, pp. 750-752, July 2001.

[9] J. P. Wang, B. S. Robinson, S. A. Hamilton, and E. P. Ippen, "Demonstration of Packet Routing Using All-optical Header Processing," IEEE Photonics Technology Letters, vol. 18, no. 21, pp. 2275-2277, Nov. 2006.

[10] F. Ramos, E. Kehayas, M. J. Martinez, R. Clavero, J. Marti, L. Stampoulidis, D. Tsiokos, H. Avramopoulos, J. Zhang, V.P. Holm-Nielsen, N. Chi, P. Jeppesen, N. Yan, T.I. Monroy, A.M.J. Koonen, M.T. Hill, Y. Liu, H.J.S. Dorren, R. Van Caenegem, D. Colle, M. Pickavet, and B. Riposati, "IST-LASAGNE: Towards All-Optical Label Swapping Employing Optical Logic Gates and Optical Flip-Flops," IEEE/OSA J. Lightwave Technology, vol. 23, no. 10, pp. 2993-3011, Oct. 2005.

[11] R. H. Walden, "Analog-to-digital converter: survey and analysis," IEEE J. Select. Areas in Communications, vol. 17, no. 4, pp. 539‑550, Apr. 1999.

[12] G. C. Vally, "Photonic analog-to-digital converters," Optics Express, vol.15, no. 5, pp.1955-1982, Feb. 2007.

[13] K. Poulton, R. Neff, B. Setterberg, B. Wuppermann, T. Kopley, R. Jewett, J. Pemillo, C. Tan, A. Montijo, "A 20GS/s 8b ADC with 1MB Memory in 0.18us CMOS," in proc. IEEE International Solid-State Circuits Conference (ISSCC), vol. 1, pp. 318-496, Feb 2003.

[14] P. J. Delfyett, T. Yilmaz, C. DePriest, A. Braun, J. Abeles, "Timing jitter in modelocked semiconductor diode lasers," in proc. IEEE Lasers and Electro-Optics Society, LEOS 2002. The 15th Annual Meeting of the IEEE, vol. 1, pp.335-336, Nov. 2002.

[15] G. P. Agrawal, "*Nonlinear fiber optics 4th ed.*": San Diego: Academic press, 2006.

[16] T. Yamamoto, E. Yoshida, and M. Nakazawa, "Ultrafast nonlinear optical loop mirror for demultiplexing 640Gbit/s TDM signals," IEE Electronics Letters, vol. 34, no. 10, pp. 1013-1014, May 1998.

[17] T. Morioka, H. Takara, S. Kawanishi, T. Kitoh and M. Saruwatari, "Error-free 500Gbit/s

all-optical demultiplexing using low-noise, low-jitter supercontinuum short pulses," IEE Electronics Letters, vol. 32, no. 9, pp. 833-834, Apr. 1996.

[18] T. R. Clark, Jr. and M. L. Dennis "Toward a 100-GSample/s Photonic A-D Converter," IEEE Photonics Letters, vol. 13, no. 3, pp. 236-238, Mar. 2001.

[19] M. Skold, M. Westlund, H. Sunnerud, and P. A. Andrekson, "100Gsamples/s optical real-time sampling system with Nyquist-limitted bandwidth," in proc. 33rd European Confference and Exhibition on optical Communication, vol. 6, PD 1.1, pp. 55-56, Sept. 2007.

[20] Y. Han, O. Boyraz, and B. Jalali, "Tera-sample per second real-time waveform digitizer," Appl. Phy. Lett., vol. 87, pp. 241116, Dec. 2005.

[21] H. F. Taylor, "An optical analog-to-digital converter--design and analysis," IEEE J. Quantum Electron., vol. 15, pp. 210-216, Apr. 1979.

[22] J. -M.Jong, M. E. Marhic, "All-optical analog-to-digital and digital-to-analog conversion implemented by a nonlinear fiber interferometer," Optics Communications, vol. 91, pp.115-112, Feb. 1992.

[23] A. Bogoni, M. Scaffardi, P. Ghelfi, and L. Poti, "Nonlinear optical loop mirrors: investigation solution and experimental validation for undesirable counterpropagating effects in all-optical signal processing," IEEE J. Quantum Electron. vol. 10, no. 5, pp. 1115-1123, Sept.-Oct. 2004.

[24] K. Ikeda, J. M. Abdul, S. Namiki, and K. Kitayama, "Optical quantizing and coding for ultrafast A/D conversion using nonlinear fiber-optic switches based on Sagnac interferometer," Optics Express, vol.13, Issue 11, pp. 4296-4302, May 2005.

[25] K. Ikeda, J. M. Abdul, H. Tobioka, S. Namiki, and K. Kitayama, "Design Considerations of All-Optical A/D Conversion: Nonlinear Fiber-Optic Sagnac Loop Interferometer-based Optical Quantizing and Coding," IEEE/OSA J. Lightwave Technology. vol. 24, no. 3, pp. 2618-2628, July 2006.

[26] Q. Wang, G. Zhu, H. Chen, J. Jaques, J. Leuthold, Al B. Piccirilli, and N. K. Dutta, "Study of All-Optical XOR Using Mach-Zehnder Interferometer and Differential scheme," IEEE J. Quantum electron., vol. 40, no. 6, pp. 703-710, June 2004.

[27] J. M. Jeong and M. E. Marhic, "All-optical logic gates based on cross-phase modulation in a nonlinear fiber interferometer," Optics Communications, vol. 85, no. 5-6, pp. 430-436, Oct. 1991.

[28] A. Bogoni, L. Poti, R.Proietti, G. Meloni, F. Ponzini, and P. Ghelfi, "Regenerative and Reconfigurable all-optical logic gates for ultra-fast applications," IEE Electronics Letters, vol. 41, no. 7, pp. 435-436, Mar. 2005.

[29] Z. Li, and G. Li, "Ultrahigh-Speed Reconfigurable Logic Gates Based on Four-Wave Mixing in a Semiconductor Optical Amplifier," IEEE Photonics Technology Letters, vol. 18, no. 12, pp. 1341-1343, June 2006.

[30] T. Sakamoto, and K. Kikuchi, " Nonlinear optical loop mirror with an optical bias controller for achieving full-swing operation of gate switching," IEEE Photonics Technology Letters, vol. 16, no. 2, pp. 545-547, Feb. 2004.

[31] S. Arahira, and Y. Ogawa," 160-gb/s OTDM signal source with 3R function utilizing ultrafast mode-locked laser diodes and modified NOLM" IEEE Photonics Technology Letters, vol. 17, no. 5, pp. 992-994, May 2005.

[32] T. Inoue, J. Hiroishi, R. Miyabe, N. Kumano, M. Takahashi, M. Sakano, T. Yagi, and Y. Mimura, " Pulse compression techniques using highly nonlinear fibers," in proc. Conference on laser and Electro optics (CLEO2007), CThQ1, May 2007.

List of Publications

I. Journals

1. Yuji Miyoshi, Kensuke Ikeda, Hideaki Tobioka, Takashi Inoue, Shu Namiki and Ken-ichi Kitayama, "All-Optical Analog-to-Digital Conversion Using Split-and-Delay Technique," IEEE/OSA Journal of Lightwave Technology, vol. 25, no. 6, pp. 1339-1347, June 2007.

2. Yuji Miyoshi, Kensuke Ikeda, Hideaki Tobioka, Takashi Inoue, Shu Namiki, and Ken-ichi Kitayama, "Ultrafast all-optical logic gate using a nonlinear optical loop mirror based multi-periodic transfer function," Optics Express, vol. 16, Issue. 4, pp. 2570-2577, Feb. 2008.

II. International Conferences

1. Kensuke Ikeda, Yuji Miyoshi, Hideaki Tobioka, Takashi Inoue, Shu Namiki and Ken-ichi Kitayama, "Split-and-Delay Technique for Simplified High-Resolution All-Optical A/D Conversion Based upon Nonlinear Fiber-Optic Switch," in proc. The 31st European Conference on Optical Communications (ECOC), Mo.3.5.4, Glasgow, Scotland, Sept. 2005.

2. Yuji Miyoshi, Kensuke Ikeda, Hideaki Tobioka, Takashi Inoue, Shu Namiki and Ken-ichi Kitayama, "Versatile all-optical logic gate using nonlinear optical loop mirror based multi-periodic transfer function," in proc. The 32nd European Conference on Optical Communications (ECOC), We 4.3.6, Cannes, France, Sept. 2006.

3. Yuji Miyoshi, Hideaki Tobioka, Takashi Inoue, Shu Namiki and Ken-ichi Kitayama, "Multi-period NOLM design for ultrafast all-optical A/D conversion," in proc. The 33rd European Conference on Optical Communications (ECOC), Tu 5.3.3, Berlin, Germany, Sept. 2007.

4. Yuji Miyoshi, Kensuke Ikeda, Hideaki Tobioka, Takashi Inoue, Shu Namiki and Ken-ichi Kitayama, "Photonic A/D conversion using NOLM," invited workshop on IEEE MTT-S International Microwave Symposium (IMS), WMK, Honolulu, Hawaii, June 2007.

III. Domestic Conferences

1. Yuji Miyoshi, Kensuke. Ikeda, Hideaki Tobioka, Takashi Inoue, Shu Namiki, and Ken-ichi. Kitayama, " Simplification of All-Optical Analog-to-Digital Converter Using Split-and-Delay Technique, "in Tech. Rep. IEICE Conf. on Optical Communication System, OCS 2005-44, pp. 51-56, Aug. 2008.

2. Yuji Miyoshi, Seiki Takagi, Hiroshi Nagaeda, Shu Namiki, and Ken-ichi Kitayama, "Multi-period NOLM for ultrafast all-optical A/D converter," in Tech. Rep. IEICE Conf. on Photonic Network, PN 2007-86, pp. 69-73, Mar. 2008.

IV. Patents

1. Yuji Miyoshi, Kensuke Ikeda, and Ken-ichi Kitayama, "Optical logic operation technique and its implemention", Japanese published patent application 2006-108980, or Tokukai 2007-279599.

2. Yuji Miyoshi and Ken-ichi Kitayama, "Optical analog-to-digital conversion technique and its implemention", Japanese published patent application 2006-248580, or Tokukai 2008-70563.

3. Hideaki Tobioka, Yuji Miyoshi, Takashi Inoue, Shu Namiki and Ken-ichi Kitayama, "Optical analog-to-digital conversion device", Japanese published patent application 2006-274947, or Tokukai 2008-96493.

4. Shu Namiki, Yuji Miyoshi, Hideaki Tobioka, Takashi Inoue, and Ken-ichi Kitayama, "Photonic waveform digitizer", Japanese published patent application 2007-020538.

5. Takashi Inoue, Hideaki Tobioka, Yuji Miyoshi, Shu Namiki, and Ken-ichi Kitayama, "Nonlinear optical loop mirror", Japanese published patent application 2007-047732.